Shear-driven formation of olivine veins by dehydration of ductile serpentinite: a numerical study with implications for transient weakening

Stefan Markus Schmalholz[1,1], Evangelos Moulas[2,2], Ludovic Räss[3,3], and Othmar Müntener[1,1]

[1]University of Lausanne
[2]Johannes Gutenberg University of Mainz
[3]ETH Zurich

November 30, 2022

Abstract

Serpentinite subduction and the associated formation of dehydration veins is important for subduction zone dynamics and water cycling. Field observations suggest that en-échelon olivine veins in serpentinite mylonites formed by dehydration during simultaneous shearing of ductile serpentinite. Here, we test a hypothesis of shear-driven formation of dehydration veins with a two-dimensional hydro-mechanical-chemical numerical model. We consider the reaction antigorite + brucite = forsterite + water. Shearing is viscous and the shear viscosity decreases exponentially with porosity. The total and fluid pressures are initially homogeneous and in the antigorite stability field. Initial perturbations in porosity, and hence viscosity, cause fluid pressure perturbations. Dehydration nucleates where the fluid pressure decreases locally below the thermodynamic pressure defining the reaction boundary. Dehydration veins grow during progressive simple-shearing in a direction parallel to the maximum principal stress, without involving fracturing. The porosity evolution associated with dehydration reactions is controlled to approximately equal parts by three mechanisms: volumetric deformation, solid density variation and reactive mass transfer. The temporal evolution of dehydration veins is controlled by three characteristic time scales for shearing, mineral-reaction kinetics and fluid-pressure diffusion. The modelled vein formation is self-limiting and slows down due to fluid flow decreasing fluid pressure gradients. Mineral-reaction kinetics must be significantly faster than fluid-pressure diffusion to generate forsterite during vein formation. The self-limiting feature can explain the natural observation of many, small olivine veins and the absence of few, large veins. We further discuss implications for transient weakening during metamorphism and episodic tremor and slow-slip in subduction zones.

Shear-driven formation of olivine veins by dehydration of ductile serpentinite: a numerical study with implications for transient weakening

Stefan M. Schmalholz[1], Evangelos Moulas[2], Ludovic Räss[3,4] and Othmar Müntener[1]

[1]Institute of Earth Sciences, University of Lausanne, 1015 Lausanne, Switzerland

[2]Institut of Geosciences and Mainz Institute of Multiscale Modeling (M[3]ODEL), Johannes Gutenberg University of Mainz, Germany

[3] Laboratory of Hydraulics, Hydrology and Glaciology (VAW), ETH Zurich, Zurich, Switzerland

[4]Swiss Federal Institute for Forest, Snow and Landscape Research (WSL), Birmensdorf, Switzerland

Email, corresponding author: Stefan Schmalholz (stefan.schmalholz@unil.ch)

Evangelos Moulas: evmoulas@uni-mainz.de; Ludovic Räss: luraess@ethz.ch;

Othmar Müntener: Othmar.Muntener@unil.ch

Key points:

- During viscous simple-shearing of serpentinite, en-échelon olivine veins form by dehydration and grow in direction parallel to compression
- Vein formation is a self-limiting process and kinetic reaction rate must be faster than fluid-pressure diffusion rate to form olivine
- Porosity evolution is controlled by three mechanisms: volume change, temporal solid density variation and reactive mass transfer

Abstract

Serpentinite subduction and the associated formation of dehydration veins is important for subduction zone dynamics and water cycling. Field observations suggest that en-échelon olivine veins in serpentinite mylonites formed by dehydration during simultaneous shearing of ductile serpentinite. Here, we test a hypothesis of shear-driven formation of dehydration veins with a two-dimensional hydro-mechanical-chemical numerical model. We consider the reaction antigorite + brucite = forsterite + water. Shearing is viscous and the shear viscosity decreases exponentially with porosity. The total and fluid pressures are initially homogeneous and in the antigorite stability field. Initial perturbations in porosity, and hence viscosity, cause fluid pressure perturbations. Dehydration nucleates where the fluid pressure decreases locally below the thermodynamic pressure defining the reaction boundary. Dehydration veins grow during progressive simple-shearing in a direction parallel to the maximum principal stress, without involving fracturing. The porosity evolution associated with dehydration reactions is controlled to approximately equal parts by three mechanisms: volumetric deformation, solid density variation and reactive mass transfer. The temporal evolution of dehydration veins is controlled by three characteristic time scales for shearing, mineral-reaction kinetics and fluid-pressure diffusion. The modelled vein formation is self-limiting and slows down due to fluid flow decreasing fluid pressure gradients. Mineral-reaction kinetics must be significantly faster than fluid-pressure diffusion to generate forsterite during vein formation. The self-limiting feature can explain the natural observation of many, small olivine veins and the absence of few, large veins. We further discuss implications for transient weakening during metamorphism and episodic tremor and slow-slip in subduction zones.

Plain language summary

Serpentinite is a rock that contains water which is bound within the crystal lattice. When serpentinite is plunging together with tectonic plates into the Earth mantle, the changing pressure and temperature conditions cause chemical reactions which releases the water bound in the crystal lattice; a process called dehydration. A typical mineral that forms by dehydration is olivine. Dehydration is important for the global water cycle, since much water is transferred with tectonic plates into the mantle and is migrating back to the Earth surface after dehydration. However, many aspects of the water cycle remain still unclear, since dehydration during plunging of tectonic plates involves the incompletely understood interaction of three fundamental mechanical and chemical processes: mechanical deformation of the rock, porous flow of released fluid and chemical reactions involving changes in rock density. Here, we present a new mathematical model to investigate the coupled processes of rock deformation, fluid flow and dehydration reactions. We present computer simulations which can explain why the dehydration occurs in narrow and elongated regions which are termed veins. We propose that our simulations could explain the observation of many small olivine veins in strongly sheared serpentinite.

1. Introduction

The dehydration of serpentinite at subduction zones is an important process for the global water cycle (e.g., Peacock, 1990; Pettke and Bretscher, 2022; Ulmer and Trommsdorff, 1995; Rupke et al., 2004), for the dynamics and seismicity at subduction zones (e.g., Bloch et al., 2018; Hacker et al., 2003) or for arc magmatism due to hydration of the mantle wedge (e.g., Hebert et al., 2009; John et al., 2012). More generally, the interaction of mineral reactions, fluid flow and rock deformation is important for a variety of geodynamic processes, such as chemical and volatile cycling (e.g., Bebout, 2014) or reaction-induced weakening of faults and shear zones (e.g., Labrousse et al., 2010; Sulem and Famin, 2009), as well as for practical applications such as natural carbon storage (e.g., Matter and Kelemen, 2009) or geothermal energy exploitation (e.g., Pandey et al., 2018). However, many aspects of the coupling of mineral reactions, fluid flow and rock deformation are still unclear.

Indirect observations that have been attributed to serpentinite dehydration at subduction zones are aseismic episodic tremor and slow-slip (ETS) phenomena (e.g., Burlini et al., 2009; Tarling et al. 2019). These phenomena are commonly thought to result from episodic fault slip, likely facilitated or promoted by pulses of fluid release associated with fluid pressure variations (e.g., Audet et al., 2009; Connolly, 1997; Frank et al., 2015; Gomberg et al., 2010; Shelly et al., 2006; Taetz et al., 2018). For example, such slow-slip occurs on the plate interface in Cascadia at 30 to 40 km depth (e.g., Gomberg et al., 2010) and for temperatures probably between 400 and 500 °C (e.g., Tarling et al., 2019 and references therein). However, how the dehydration reaction, the associated fluid release and the volumetric and shear deformation of the involved rocks are coupled and actually cause the episodic slow-slip phenomena remains elusive.

Direct observation of the dehydration of serpentinite at subduction zones is not possible in nature. However, field observations in areas with abundant exposed serpentinites

88 at variable pressure and temperature may provide insight into incipient dehydration stages. In
89 the European Alps, exposed serpentinites, which experienced variable peak pressures and
90 temperatures, are abundant in many regions. Examples are the serpentinites of Saas Zermatt
91 (Western Alps) or of the Erro-Tobbio unit (Voltri massif, Ligurian Alps, Italy; e.g., Hermann
92 et al., 2000; Peters et al., 2020; Plümper et al., 2017; Scambelluri et al. 1991, Scambelluri et
93 al., 1995; Kempf et al., 2020). These serpentinite bearing regions are key areas that preserve
94 ductile and brittle structures that are related to fluid release. The serpentinites of the Erro-
95 Tobbio unit exhibit olivine-bearing veins and the metamorphic olivine most likely results
96 from the breakdown of antigorite and brucite (Fig. 1; e.g., Hermann et al., 2000; Plümper et
97 al., 2017; Scambelluri et al., 2004). The olivine veins occur in two settings: as minimally
98 deformed veins within little deformed, variably serpentinized peridotite and as deformed
99 veins within strongly deformed antigorite serpentinite, described as a serpentinite mylonite
100 (Fig. 1; e.g., Hermann et al., 2000; Plümper et al., 2017). These serpentinite mylonites are cut
101 by en-échelon olivine veins, which in turn are dissected by multiple sets of olivine-bearing
102 shear bands (Hermann et al., 2000). Plümper et al. (2017) suggest that the association of
103 undeformed and sheared veins attests that dehydration-induced vein formation was
104 synchronous with ductile deformation in the enclosing serpentinite mylonites. Furthermore,
105 Hermann et al. (2000) hypothesize that (i) multiple sets of olivine shear bands provide
106 evidence for continuous deformation, (ii) sheared olivine-rich veins are probably very weak
107 due to continuous solution and precipitation in the presence of a fluid phase, (iii) fluid
108 produced by the dehydration reaction was (partially) trapped in the serpentinite mylonite and
109 (iv) serpentinite mylonites are not only zones with highly localized deformation but also
110 zones of focused fluid flow. However, these coupled physical-chemical hypotheses for olivine
111 vein formation have not been tested with theoretical models based on the concepts of
112 continuum mechanics and thermodynamics. Recently, Huber et al. (2022) presented a hydro-

chemical (HC) model to study the formation of olivine veins in dehydrating serpentinite. However, they do not consider any solid-mechanical aspects of olivine vein formation and do, hence, not consider volumetric or shear deformation of the serpentinite and associated fluid pressure changes. Therefore, we cannot apply their model to test the coupled physical-chemical hypothesis of shear-driven olivine vein formation.

Here, we test the hydrological, mechanical and chemical feasibility of a hypothesis for the formation of observed olivine veins in serpentinite mylonites with a new two-dimensional (2D) hydro-mechanical-chemical (HMC) model. The hypothesis is (Fig. 2): During viscous shearing of serpentinite, the magnitudes of ambient pressure and temperature were close to the magnitudes required for triggering the dehydration reaction from serpentinite to olivine (Fig. 3A). The effective viscosity of serpentinite was spatially variable, for example due to variable porosity or heterogeneities in mineralogy (Fig. 2A). Weak domains, with lower viscosity, cause pressure variations in the sheared serpentinite so that the dehydration reactions are triggered in domains with locally decreased pressure. The dehydration forms olivine and increases the porosity locally, which in turn increases the size of weak domains, consisting of an olivine-fluid mixture. The dehydration region forms vein-like structures that grow in a direction parallel to the maximal compressive stress without any fracturing (Fig. 2A and B). After fluid has escaped the olivine-rich region, the olivine-rich veins, observable in the field, have formed (Fig. 2C). We test this hypothesis with a 2D HMC model because such models are suitable to theoretically study the coupling between chemical reactions, fluid flow and deformation (e.g., Kolditz et al., 2015; Poulet et al., 2012). Such coupled models have been applied to study a variety of geodynamic processes, for example, reaction-driven cracking during serpentinization (e.g., Evans et al., 2020), porosity evolution and clogging during serpentinization (e.g. Malvoisin et al., 2021), the impact of dehydration on earthquake nucleation (e.g., Brantut et al., 2011), the impact of shear heating and associated chemical

138 rock decomposition on thrusting (e.g., Poulet et al., 2014) or reactive melt migration (e.g.,
139 Aharonov et al., 1997; Baltzell et al., 2015; Bessat et al., 2022; Schiemenz et al., 2011). We
140 apply here an extension of a HMC model that was previously used to model the dehydration
141 reaction: brucite = periclase + water (Schmalholz et al., 2020). Here, we elaborate this HMC
142 model and consider a simple MgO-SiO_2-H_2O (MSH) system for the reaction: antigorite +
143 brucite = forsterite + water (Fig. 3). For simplicity, we consider an isothermal system and a
144 fixed chemical composition so that the reaction antigorite + brucite = forsterite + water is
145 balanced everywhere in the model domain.

146 The main aim of our study is to better understand the fundamental coupling of
147 dehydration reactions, fluid flow and rock deformation, for which a simplified model is
148 useful. Particular aims of our study are (1) to test the hypothesis for the shear-driven
149 formation of olivine veins, (2) to quantify the mechanisms that control the porosity evolution
150 and fluid pressure during dehydration of rocks and (3) to quantify the impact of shearing rate
151 and kinetic reaction rate on the growth of dehydration veins.

152

153 **2. Mathematical model**

154 *2.1. Porous medium densities*

155 We consider a simple MSH system and the reaction antigorite ($Mg_{48}Si_{34}O_{85}(OH)_{62}$) +
156 20 brucite ($Mg(OH)_2$) = 34 forsterite (Mg_2SiO_4) + 51 water (H_2O). We assume that antigorite
157 and brucite together represent one solid rock phase with a homogeneous solid density, ρ_s (in
158 kg/m^3), and homogeneous material properties. All model parameters and variables are
159 presented in Table 1. The total density of the porous rock, either consisting of antigorite +
160 brucite or forsterite + water, is

$$\rho_T = \rho_f \phi + \rho_s (1-\phi) \tag{1}$$

with porosity ϕ (volume ratio) and pore-fluid density ρ_f. For simplicity, we assume that the solid phase consists of two components, (1) the non-volatile components, MgO and SiO_2, that remain always in the solid and (2) the volatile component, H_2O, that is liberated during dehydration. We quantify the amount of the non-volatile component as a function of MgO inside the solid with its solid mass (in kg) fraction, X_s, which is $X_s = 0.74$ (68 times the molar mass of MgO / (68 times the molar mass of MgO + 51 times the molar mass of H_2O)) for the solid made of antigorite + brucite in a molar ratio of 1/20. Equivalently, $X_s = 1$ for forsterite. We neglect the SiO_2 in the calculations, because the SiO_2 for the considered reaction cannot vary independently from MgO. The relative density of the solid MgO component in the solid phase is

$$\rho_X = \rho_s X_s \tag{2}$$

2.2. Hydro-chemical model

The conservation of mass (per unit volume) of the solid and the fluid is given by respectively (e.g., McKenzie, 1984)

$$\frac{\partial\left(\rho_s (1-\phi)\right)}{\partial t} + \nabla\left[\rho_s (1-\phi)\,\mathbf{v}^s\right] = -\Gamma \tag{3}$$

$$\frac{\partial\left(\rho_f \phi\right)}{\partial t} + \nabla\left[\rho_f \phi \mathbf{v}^f\right] = \Gamma \tag{4}$$

where t is time, ∇ is the divergence operator, $\mathbf{v}^f$ and $\mathbf{v}^s$ are vectors of the fluid and solid barycentric velocities, respectively, and Γ is a dehydration rate that quantifies the rate at which mass is transferred from the solid to the fluid phase. Concerning the symbols for vector and tensor quantities, we use indices f and s as superscripts, because vector and tensor

components will have additional subscripts indicating the spatial direction, and scalar quantities can be easier distinguished from vector and tensor quantities. Here, we do not use two separate mass conservation equations for solid and fluid, but use the conservation equation of total mass which results from the sum of equations (3) and (4) (e.g., Fowler, 1985; Beinlich et al., 2020; Malvoisin et al., 2021; Plümper et al., 2016; Schmalholz et al., 2020):

$$\frac{\partial \rho_T}{\partial t} + \nabla\left[\rho_f \phi \left(\mathbf{v}^f - \mathbf{v}^s\right)\right] + \nabla\left(\rho_T \mathbf{v}^s\right) = 0 \tag{5}$$

The relative velocity of the fluid to the solid, $\mathbf{v}^f - \mathbf{v}^s$, in equation (5) is expressed by Darcy's law in the absence of gravity

$$\phi\left(\mathbf{v}^f - \mathbf{v}^s\right) = -\frac{k\phi^3}{\eta_f}\nabla p_f \tag{6}$$

where k is the permeability coefficient in a Kozeny–Carman-type permeability expression, η_f is the fluid viscosity and p_f is the fluid pressure. We need two mass conservation equations because we consider two phases, solid and fluid. In addition to the conservation of total mass, we use the conservation of the total non-volatile component (MgO) which is described by

$$\frac{\partial}{\partial t}\left[\rho_X \left(1-\phi\right)\right] + \nabla\left[\rho_X \left(1-\phi\right)\mathbf{v}^s\right] = 0\,. \tag{7}$$

There is no fluid velocity in this conservation equation because we assume that the dissolution of MgO in the fluid is negligible.

We consider a constant temperature and a closed system with constant system composition for the whole model domain, however, H_2O can migrate within our model domain. It has been experimentally demonstrated that dehydration reactions are controlled by

fluid pressure (e.g., Llana-Fúnez et al., 2012) and, therefore, we approximate ρ_s, ρ_f and X_s as a function of p_f, which is expressed as (Schmalholz et al., 2020):

$$\begin{aligned} \rho_f &= \rho_f^{EQ}\left(p_f\right) \\ \rho_s &= \rho_s^{EQ}\left(p_f\right) \\ X_s &= X_s^{EQ}\left(p_f\right) \end{aligned} \quad , \tag{8}$$

whereby the values of ρ_s^{EQ}, ρ_f^{EQ} and X_s^{EQ} for a range of values of p_f are calculated by equilibrium Gibbs free-energy minimization (e.g., Connolly, 2005, 2009; Fig. 3), using the thermodynamic dataset of Holland and Powell (1998). We assume that ρ_f always corresponds to ρ_f^{EQ}, as a result of its equation of state (Fig. 3C). Due to the sharp, step-like variation of ρ_s^{EQ} and X_s^{EQ} with varying p_f across the dehydration reaction (Fig. 3C and D) we assume that the reaction is controlled by a kinetic reaction timescale, so that values of ρ_s do not change instantaneously if p_f crosses the value of the reaction pressure at 12.65 kbar (Fig. 3). The kinetic reaction timescales relevant to thermodynamic equilibrium are (e.g., Omlin et al., 2017)

$$\begin{aligned} \frac{\partial \rho_s}{\partial t} &= \frac{\rho_s^{EQ} - \rho_s}{t_{kin}} \\ \frac{\partial X_s}{\partial t} &= \frac{X_s^{EQ} - X_s}{t_{kin}} \end{aligned} \tag{9}$$

where t_{kin} is the characteristic kinetic timescale. Employing an effective kinetic timescale for the considered reaction allows us to quantify the impact of reaction kinetics on the model results. Furthermore, the simulations are numerically more stable because the kinetic formulation resolves better the temporal transition of the reaction and prohibits potentially

strong density oscillations for numerical grid points where values of p_f are very close to the reaction pressure.

2.3. Mechanical model

The solid part of the 2D porous medium is behaving in a visco-plastic manner under shear deformation. We assume that the shear viscosity is an exponential function of the porosity (e.g., Schmeling et al., 2012). There are other possible porosity-viscosity relations, but for simplicity we apply here only one of these relations. The relations between the deviatoric stress tensor components, $\tau_{ij} = \sigma_{ij} + p\delta_{ij}$ (where σ_{ij} are the components of the total stress tensor, p is total pressure and δ_{ij} is the Kronecker delta) and solid velocity gradients, or deviatoric strain rate tensor components D_{ij}, are then

$$\tau_{ij} = 2\eta_{s0} \exp\left[-30\left(\varphi - \varphi_0\right)\right] D_{ij} = 2\eta_s D_{ij} \tag{10}$$

where subscripts i and j are either 1 (representing the horizontal x-direction) or 2 (representing the vertical y-direction), η_{s0} is the reference solid shear viscosity for the initial porosity, φ_0, and $D_{ij} = \left(\partial v_i^s / \partial x_j + \partial v_j^s / \partial x_i\right)/2 - \delta_{ij}\left(\partial v_i^s / \partial x_i\right)/3$. The η_s represents the effective, porosity-dependent shear viscosity of the porous rock. The factor 30 was determined by experiments with olivine-melt mixtures (e.g., Schmeling et al., 2012). We further apply for one simulation a von Mises yield stress, τ_y, to limit the maximal value of the deviatoric stresses. The square root of the second invariant of the deviatoric stress tensor, $\tau_{II} = \sqrt{0.5\left(\tau_{xx}^2 + \tau_{yy}^2\right) + \tau_{xy}^2}$ controls a plastic multiplier, $\vartheta = 1 - \tau_y / \tau_{II}$. If $\vartheta > 0$, then deviatoric stresses are modified using

$$\tau_{ij} = (1-\vartheta)\,\tau_{ij}\,. \tag{11}$$

This von Mises plasticity prohibits that stresses locally increase to unrealistically high values. Furthermore, we consider a poro-visco-elastic volumetric deformation for which the divergence of the solid velocity field is a function of total pressure, p, and fluid pressure, p_f (e.g., Yarushina and Podladchikov, 2015):

$$\nabla \mathbf{v}^s = -\frac{1}{K_d}\left(\frac{dp}{dt} - \alpha\frac{dp_f}{dt}\right) - \frac{p-p_f}{(1-\phi)\,\lambda} \tag{12}$$

where λ is the bulk viscosity, K_d is the drained bulk modulus, and $\alpha = 1 - K_d / K_s$ with K_s being the solid bulk modulus. The applied equations for conservation of total linear momentum (or force balance equations) without inertial forces and gravity are

$$\nabla \sigma_{ij} = 0 \tag{13}$$

2.4. Governing system of equations

The above equations represent a system of 11 equations for 11 unknowns, which are p_f, ϕ, ρ_s, ρ_f, X_s, p, v_x^s, v_y^s, τ_{xx}, τ_{yy} and τ_{xy}, assuming that the deviatoric stress tensor is symmetric, $\tau_{xy} = \tau_{yx}$. The deviatoric stress tensor components, τ_{xx}, τ_{yy} and τ_{xy}, are calculated using equations (10). The solid and fluid densities and the mass fraction are calculated from the fluid pressure using equation (8) (see also equation (16) below and Fig. 3C and D). Equation (5) is used to determine the fluid pressure, p_f, equation (12) to determine total pressure, p, equation (7) to determine the porosity, ϕ, and the two force balance equations (13) to determine the two solid velocities, v_x^s and v_y^s. To determine p_f, p, ϕ, v_x^s and v_y^s we employ the iterative pseudo-transient (PT) finite difference method described in detail in Schmalholz et al. (2020). The PT equations are

$$
\begin{aligned}
\frac{\Delta^{PT} p_f}{\Delta t_{pf}^{PT}} &= -\frac{\partial \rho_T}{\partial t} + \nabla\left[\rho_f \frac{k\phi^3}{\eta_f}\nabla p_f\right] - \nabla\left(\rho_T \mathbf{v}^s\right) \\
\frac{\Delta^{PT} \phi}{\Delta t_{\varphi}^{PT}} &= \frac{\partial}{\partial t}\left[\rho_X (1-\phi)\right] + \nabla\left[\rho_X (1-\phi)\mathbf{v}^s\right] \\
\frac{\Delta^{PT} v_i^s}{\Delta t_v^{PT}} &= \nabla \sigma_{ij} \\
\frac{\Delta^{PT} p}{\Delta t_p^{PT}} &= -\nabla \mathbf{v}^s - \frac{1}{K_d}\left(\frac{dp}{dt} - \alpha\frac{dp_f}{dt}\right) - \frac{p - p_f}{(1-\phi)\lambda}
\end{aligned}
\qquad (14)
$$

When the discrete PT time derivatives of the left-hand sides of the equations (14) converge towards zero during iterations, then the corresponding steady-state equations on the right-hand sides are solved. The closed system of governing equations is given by equations (8), (10), (12) and (14).

2.5. Model configuration

We assume that p_f and p are initially identical. The porosity is 2%, except in an elliptical region in the model center where the porosity exhibits a Gaussian distribution with a maximal value of 16% (Fig. 4). The initial Gaussian distribution of the porosity is: $\phi_0 = 0.02 + 0.14\exp\left[-\left(x/r\right)^2 - \left(y/2r\right)^2\right]$. The distance r controls the width, or variance, of the porosity distribution which has an elliptical form with an axis ratio of 2 and with the long axis parallel to the vertical y-direction (Fig. 4). The origin of the coordinate system is at the center of the elliptical region with positive coordinates indicating towards the right side and upwards (Fig. 4). The shear and bulk viscosities are smaller in the central region due to the higher porosity. We assume a constant temperature of 500 °C for which the thermodynamic reaction pressure in our model is at 12.65 kbar (Fig. 3). The exact temperature value is not essential for our isothermal study, because the variation of the solid and fluid densities with

varying fluid pressure is similar for temperatures between 450 and 550 °C (Fig. 3A and B). The initial values of p_f and p are everywhere equal to 12.75 kbar, which is a pressure value slightly above the thermodynamic reaction pressure (Fig. 3A and B). We apply far-field simple shear for the boundary velocities (Fig. 4) so that the divergence, or volume change, of the entire model domain is zero. Shearing is parallel to the horizontal x-direction and, hence, orthogonal to the long axis of the elliptical region with elevated porosity (Fig. 4). Boundary conditions for ϕ and p_f are of Dirichlet type, with boundary values fixed to the initial ambient values.

2.6. Numerical algorithm and dimensionless parameters

All partial derivatives are approximated with discrete difference ratios following the standard procedure of staggered finite difference (FD) methods (e.g., Gerya, 2019). The numerical algorithm consists of an outer time loop containing an internal PT iteration loop (Schmalholz et al., 2020). The PT iteration procedure aims at minimizing the PT time derivatives, i.e. the left-hand sides in the discretized equations (14). The iteration procedure is stopped when the PT time derivatives reach a predefined tolerance, here 10^{-8}. The iterative implicit PT solution of the discretised system of equations (14) requires the definition of four numerical pseudo time steps, Δt^{PT}, namely, Δt_{pf}^{PT}, Δt_{p}^{PT}, Δt_{ϕ}^{PT}, and Δt_{v}^{PT} to solve for p_f, p, ϕ, and v_x^s and v_y^s, respectively. The physical time step, Δt, controls the evolution of the system in physical time for which we implicitly solve. The applied numerical time steps are specified in appendix A1.

There are many possibilities to scale and non-dimensionalize the model parameters inside the numerical algorithm. We programmed the numerical algorithm in such a way that the

specific magnitudes of individual parameters, such as shear viscosity, are not significant and that the characteristic physical behaviour of the system is controlled by dimensionless parameters. This scaling provided also the most stable convergence during the PT iterations. The applied dimensionless parameters and numerical examples applied in the simulations are:

$$
\begin{aligned}
&\Omega_1 = \frac{w}{r} && e.g. \quad \Omega_1 = \frac{4m}{10^{-1}m} = 40 \\
&\Omega_2 = \frac{k}{\eta_f}\frac{\eta^s}{r^2} && e.g. \quad \Omega_2 = \frac{10^{-22}m^2}{10^{-3}Pas}\frac{10^{18}Pas}{\left(10^{-1}m\right)^2} = 10 \\
&\Omega_3 = \frac{\lambda}{\eta^s} && e.g. \quad \Omega_3 = \frac{2\times10^{18}Pas}{10^{18}Pas} = 2 \\
&\Omega_4 = \frac{\bar{D}_{xy}\eta^s}{p_{ini}} && e.g. \quad \Omega_4 = \frac{1.12\times10^{-10}s^{-1}10^{18}Pas}{12.75\times10^{8}Pa} = 0.0878
\end{aligned}
\tag{15}
$$

where w is the model width and $\bar{D}_{xy}$ is the applied far-field simple shear rate (Fig. 4). The values of the applied parameters are discussed in section 4.

For reasons of numerical efficiency, we approximate the thermodynamic relations of the densities and mass fractions with the fluid pressure, obtained with Gibbs free-energy minimization, with analytical functions (Fig. 3C and D):

$$
\begin{aligned}
&\rho_f = 1194\times\ln\left(\frac{p_f}{p_{ini}}+1\right)^{1/3.5} \\
&\rho_s = -\tanh\left(600\times\frac{p_f - p_R}{p_{ini}}\right)\times323.32 + 2848 + \left(\frac{p_f}{p_{ini}} - 0.0078\right)\times30.4762 \\
&X_s = -\tanh\left(600\times\frac{p_f - p_R}{p_{ini}}\right)\times0.1292 + 0.8707
\end{aligned}
\tag{16}
$$

where p_R is the reaction pressure, here 12.65 kbar. We use the functions above in the numerical algorithm to calculate densities and mass fraction from the current fluid pressure.

316 **3. Results**

317 *3.1. Scaling and presentation of results*

318 We present most quantities in dimensionless form to emphasize their general validity. For
319 example, all distances are made dimensionsless by dividing them by r and all times are made
320 dimensionless by dividing them with the characteristic time $t_c = r^2\eta_f / (k K_s)$. Consequently,
321 all velocities are made dimensionless by dividing them by the characteristic velocity r / t_c. In
322 contrast, since we consider a particular metamorphic reaction, we display the densities and
323 pressures in dimensional units.

324 *3.2. Dehydration vein formation under simple shear*

325 For the first simulation presented here, we use the dimensionless parameters and
326 specific parameter values given in equation (15) . The numerical resolution is 900×900 grid
327 points in the x- and y-direction, respectively. A numerical resolution test is given in appendix
328 A2. The coupling of the dehydration reaction, fluid flow and solid deformation is controlled
329 by four characteristic time scales: a time scale related to fluid pressure diffusion,
330 $t_{dif} = r^2\eta_f / (k\varphi_0^3 K_s)$, a time scale related to the applied far-field deformation, $t_{def} = 1/\bar{D}_{xy}$, a
331 time scale related to the mineral-reaction kinetics, t_{kin} (equation (9)), and a time scale related
332 to viscoelastic stress relaxation, $t_{rel} = \eta_s / K_s$. We assume here $K_s = 10^{11}$ Pa which, for the
333 parameter values in equation (15), yields $t_{rel} / t_{def} \sim 10^{-3}$ and indicates that the deformation is
334 effectively viscous since t_{rel} is significantly shorter than t_{def}. The ratio t_{rel} / t_{def} is commonly
335 referred to as Deborah number (e.g. Reiner, 1964; Moulas et al., 2019). For the first
336 simulation, $t_{def} / t_{dif} = 0.071$ and $t_{kin} / t_{dif} = 0.0025$ so that both the characteristic times for
337 shearing and reaction kinetics are shorter than the characteristic time of diffusive fluid flow.

338 The ratio t_{kin} / t_{dif} is similar to a Damköhler number since it relates the characteristic time of
339 mineral reactions to the characteristic time of transport by diffusive fluid flow. The central
340 region with initially higher porosity (Fig. 5E) represents a mechanically weak inclusion
341 because the shear and bulk viscosity decrease with increasing porosity. The applied far-field
342 simple shear causes variations in p_f around the weak region and the numerical results for the
343 first time step show two regions in which p_f is smaller than the reaction pressure of 12.65
344 kbar (black contours in Fig. 5A). Therefore, dehydration is triggered in these two regions of
345 decreased p_f. The dehydration causes the release of water, consequently an increase in
346 porosity and, hence, a decrease of viscosity. With progressive simple shearing these
347 dehydrating regions grow in the direction parallel to the maximal principal stress, σ_1, which
348 is oriented 45 degrees with respect to the shearing direction (Fig. 5E). The maximal and
349 minimal, σ_3, principal stresses have been calculated using the algorithm of Spitz et al. (2020),
350 which was originally developed to calculate principal strain directions. During progressive
351 shearing, two dehydrating regions evolve and form vein-like regions with increased values of
352 ρ_s and ϕ (Fig. 5). The total solid velocity field (grey arrows in Fig. 5A to D) indicates the
353 applied far-field simple shear and local deviations from the horizontal shear direction. For the
354 specific parameters given in equation (15) the maximal shear stresses are ca. 125 MPa. We
355 also calculate the distance between the highest (in vertical y-direction) and the lowest point on
356 the contours for p_f = 12.65 kbar (red straight lines in Fig 5A to D). We will use this distance
357 as a proxy for the change in length of the dehydrating region representing the length of the
358 dehydration vein. During progressive shearing, the value of ρ_s in the dehydration region
359 increases from initially ca. 2550 kg m^{-3} to ca. 3100 kg m^{-3} which represents the transformation
360 from antigorite + brucite to forsterite (Figs. 3C and 5A to D). In the region of the two
361 forsterite veins, the associated values of ϕ increase from initially 2% to ca. 60% (Fig. 5E to

362 H). Two representative contours of ϕ, for 5 and 15%, highlight two features of the evolution
363 of ϕ: the growth of high-porosity dehydration veins and the clock-wise rotation of the initial
364 porosity field due to the applied simple shear (Fig. 5E to H).

365

366 *3.3. Dehydration vein formation for faster deformation rate and plastic yield stress*

367 We perform a second simulation with the same parameters as the first simulation, except that
368 we apply now a different value of t_{def} which provides t_{def} / t_{dif} = 0.038 (Fig. 6A to D)
369 generating a faster shearing since the characteristic time of deformation is shorter. The main
370 difference to the simulation with t_{def} / t_{dif} = 0.071 (Fig. 5) is that the two dehydration regions
371 connect during progressive shearing to form a single dehydration vein (Fig. 6D). For the
372 specific parameters given in equation (15) the maximal shear stresses are ca. 220 MPa. We
373 perform a third simulation with the same parameters as in the second simulation and apply a
374 von Mises yield stress of 150 MPa (Fig. 6E to H). With such yield stress, a single dehydration
375 vein also forms but the vein is shorter and thicker for the same simulated times (Fig. 6). The
376 performed three simulations result in a similar development of dehydration veins with
377 forsterite, but show that different deformation rates and the application of a yield stress impact
378 the geometry and length of the veins.

379

380 *3.4. Coupling of dehydration reaction, fluid flow and solid deformation*

381 To better understand and visualize the coupling between the dehydration reaction, fluid flow
382 and solid deformation we show the distribution and evolution of various quantities on a single
383 figure (Fig. 7). We use the results of the first simulation (Fig. 5) and we focus on one
384 dehydration region in the area to the top-left of the model center (Fig. 7). The divergence of

385 the solid velocity, $\nabla \mathbf{v}^s = \partial v_x^s / \partial x + \partial v_y^s / \partial y$, indicates a volumetric change associated with
386 dehydration vein formation (Fig. 7). A positive value of $\nabla \mathbf{v}^s$ indicates volume increase, or
387 dilation (blue colors in Fig. 7). Overall, the solid velocities indicate the applied far-field
388 simple shear deformation (blue arrows in Fig. 7), with some deviations around the
389 dehydrating region. The fluid velocities (red arrows in Fig. 7) are completely different
390 compared to the solid velocities. For the first time step, fluid flow only occurs in the central
391 region where the porosity, and hence permeability, is high (Fig. 7A). During dehydration vein
392 formation, fluid flow mainly occurs in the region of the veins where significant dilation takes
393 places (Fig. 7B to D). The fluid velocities indicate fluid flow from the boundary of the
394 dehydrating region towards the centre of the vein (Fig. 7C). In other words, fluid is released
395 during dehydration from the surrounding serpentinite and the released fluid flows into the
396 vein. For the first time step, the porosity distribution indicates the initial, Gaussian-type,
397 porosity distribution (blue contours in Fig. 7). With progressive deformation and vein
398 formation, the high-porosity region grows in the direction of the dehydration vein, indicated
399 by significant dilation and fluid flow. At the beginning of shearing, a larger region with fluid
400 pressure (red contours in Fig. 7) <12.65 kbar corresponds more or less to the region of
401 significant dilation (Fig. 7A). The solid densities (dashed grey contours in Fig. 7) increase
402 during the progressive dehydration reaction and the transformation from antigorite + brucite
403 to forsterite (Fig. 7B to D). The values of solid density increase with time due to the applied
404 mineral-reaction kinetics which avoids that the density changes instantaneously once the fluid
405 pressure decreases locally below 12.65 kbar. With progressive vein formation, fluid pressures
406 below 12.65 kbar only exist in the region of significant dilation, fluid flow and increased
407 values of solid density (Fig. 7).
408

3.5. Mechanisms controlling porosity variation and fluid pressure

In our coupled HMC model, the temporal variation of porosity is controlled by several mechanisms, such as volumetric deformation of the solid or mass transfer due to the dehydration reaction. To quantify the relative contribution of the mechanisms controlling the temporal variation of porosity, we post-process our numerical results (i.e. calculate values from saved numerical results). We quantify the mass transfer rate, Γ, associated with the dehydration reaction, which can be expressed by (using equation (3)):

$$\Gamma = -\frac{d\left(\rho_s\left(1-\phi\right)\right)}{dt} - \rho_s\left(1-\phi\right)\nabla\mathbf{v}^s . \tag{17}$$

Note that in equation (17) the material time derivative (d/dt, including the advection term, $\mathbf{v}^s\nabla\left[\rho_s\left(1-\phi\right)\right]$) is used and, hence, the divergence term is different compared to equation (3) . Therefore, equation (17) represents an approximation of Γ since the advective term is not taken into account, here for simplicity of the post-processing. Equation (17) can be rearranged to provide an expression for the temporal variation of the porosity:

$$\frac{1}{\left(1-\phi\right)}\frac{d\phi}{dt} = \nabla\mathbf{v}^s + \frac{1}{\rho_s}\frac{d\rho_s}{dt} + \frac{\Gamma}{\rho_s\left(1-\phi\right)} \tag{18}$$

Equation (18) shows that the temporal variation of the porosity is controlled by three mechanisms: (1) volumetric deformation of the solid (i.e. divergence of velocity field; first term on right-hand side of equation (18)), (2) temporal variation of solid density (second term) and (3) mass transfer of H_2O from the solid to the fluid phase associated with the dehydration reaction (third term). We display the spatial distribution of the four terms in equation (18) for the first simulation at a dimensionless time of 0.7 (Fig. 8). The temporal variation of porosity, quantified by the term on the left-hand side of equation (18), is positive and largest in the region of increased porosity, indicating an increase in porosity with time

(Fig. 8A). Each of the three terms on the right-hand side of equation (18) can be calculated from the saved numerical results (Fig. 8C to E) and their sum (Fig. 8B) provides essentially the same result as the term on the left-hand side of equation (18) (Fig. 8A). The results show that the magnitudes of the relative contributions of volume change (Fig. 8C), solid density variation (Fig. 8D) and mass transfer (Fig. 8E) to the temporal variation of porosity are similar. Therefore, volume change, solid density variation and mass transfer equally contribute to the porosity variation and, hence, for the evolution of the dehydration veins.

We also investigate the porosity variation for a simulation which has the same value of $t_{def} / t_{dif} = 0.071$ as the first simulation, but with a slower kinetic-reaction rate (or longer reaction time) of $t_{kin} / t_{dif} = 0.022$ for a dimensionless time of 1.0 (Fig. 9). The magnitude of the temporal porosity variation is now slower (compare Fig. 8A and 9A) but the relative contribution of volume change, solid density variation and mass transfer to the porosity variation is again similar. Therefore, different kinetic reaction rates change the magnitude of the temporal porosity variation, but do not change the relative importance of volume change, density variation and mass transfer controlling the porosity evolution.

Similar to the temporal variation of ϕ, the distribution of p_f is also controlled by several mechanisms and variables. To quantify the mechanisms controlling p_f, we post-process again our numerical results. Substituting equation (12), which defines $\nabla \mathbf{v}^s$, into equation (18) and solving for p_f yields

$$p_f = p + \frac{\lambda(1-\phi)}{K_d}\left(\frac{dp}{dt} - \alpha\frac{dp_f}{dt}\right) + \lambda\frac{d\phi}{dt} - \frac{\lambda(1-\phi)}{\rho_s}\frac{d\rho_s}{dt} - \frac{\lambda}{\rho_s}\Gamma . \qquad (19)$$

Equation (19) shows that p_f is controlled by five mechanisms and quantities: (1) the magnitude of p (first term on the right-hand side of equation (19)), (2) elastic deformation

453 involving the temporal variation of p and p_f (second term), (3) temporal variations in
454 porosity (third term), (4) temporal variations of solid density (fourth term) and (5) mass
455 transfer by dehydration (fifth term). We display the spatial distribution of all terms in equation
456 (19) for the first simulation at a dimensionless time of 0.7 (Fig. 10). The distribution of p_f is
457 mainly controlled by the distribution of p (Fig. 10A and C). The distribution of p_f can be
458 accurately post-processed by summing up the five terms on the right-hand side of equation
459 (19) (Fig. 10B). The mass transfer (Fig. 10E), the porosity variation (Fig. 10F) and the solid
460 density variation (Fig. 10G) have an approximately equal impact on the distribution of p_f,
461 but their contributions are significantly smaller compared to the contribution of p. The
462 contribution of elastic volumetric deformation (Fig. 10H) is essentially negligible, since it is
463 three orders of magnitude smaller than the magnitude of p_f. For the presented simulation, the
464 maximal value of the deviatoric stress invariant, τ_{II} (equation (11)), in the model domain is
465 ca. 140 MPa (Fig. 10D).

466

467 *3.6. Impact of kinetic reaction rate and shearing rate on vein evolution*

468 We performed in total ten simulations to investigate the impact of the far-field
469 shearing rate and of the kinetic reaction rate on the evolution of dehydration veins and
470 forsterite generation (Fig. 11). Six simulations had the same value of t_{kin} / t_{dif} = 0.0025 but
471 different values of t_{def} / t_{dif} (legend in Fig. 11A). The increase in length of the red line shown
472 in figure 5A to D is used as a proxy for the temporal evolution of the vein length (Fig. 5A).
473 The initial value of vein length is determined by the initial distribution of p_f (Fig. 5A). In
474 regions with p_f <12.65 kbar the dehydration reaction is triggered, which causes a local

475 increase of H_2O and an increase of p_f (Fig. 11B). For the six simulations, this initial increase
476 of p_f generated values of p_f >12.65 kbar everywhere in the model domain, so that the vein
477 length is zero (Fig. 11A and B). With progressive deformation, values of p_f decrease again
478 below 12.65 kbar initiating the growth of a dehydration vein. The time until values of p_f
479 decrease below 12.65 kbar is longest for the simulation with the slowest far-field deformation
480 rate (Fig. 11A). Consequently, the increase of ρ_s starts latest for the simulation with slowest
481 far-field deformation rate (Fig. 11C). However, during significant increase of ρ_s the rate of
482 increase (indicated by the slope of the density versus time lines) of ρ_s is similar for all
483 simulations, because they considered the same mineral-kinetic rate (t_{kin} / t_{dif} = 0.0025). The
484 simulation with the fastest deformation rate (Fig. 6A to D; blue line in Fig. 11A to C) was run
485 a second time, but then with a von Mises yield stress (Fig. 6E to F; dashed blue line in Fig.
486 11A to C). The application of the yield stress slows down the vein growth, but has no
487 significant impact on the evolution of ρ_s (Fig. 11C). The temporal evolution of the vein
488 length shows that the veins grow fast at the onset of vein formation and then vein growth
489 slows down progressively (Fig. 11A) because the minimum values of p_f in the model
490 increase progressively (Fig. 11B) due to ongoing fluid flow which reduces gradients of p_f.

491 We performed four simulations for the same value of t_{def} / t_{dif} = 0.071 but for four different
492 values of t_{kin} / t_{dif} (legend in Fig. 11D). The vein growth is similar for the four simulations
493 (Fig. 11D), however, the increase of ρ_s is significantly different due to the different mineral-
494 reaction rates (Fig. 11F). The values of ρ_s increase fastest for the fastest reaction rate (Fig.
495 11F), but values of p_f vary less during deformation for faster reaction rates (Fig. 11E). For
496 slow reaction kinetics, t_{kin} / t_{dif} = 0.022 (Fig. 11F), maximal values of ρ_s did not reach 2800

kg m^{-3} hindering the complete formation of forsterite when the vein growth has essentially stopped (corresponding blue line in Fig. 11D). The results for different kinetic rates suggest that the kinetic reaction rate must be significantly faster than the pressure diffusion rate to allow the complete transformation from antigorite + brucite to forsterite during dehydration and vein growth, while fluid pressures are in the forsterite stability field.

4. Discussion

The performed simulations show that it is hydrologically, mechanically and chemically feasible to form olivine veins by dehydration reactions during ductile shearing of serpentinite. In the scenario studied here, dehydration is shear-driven and triggered by fluid pressure perturbations caused by heterogeneities in porosity-dependent effective viscosity. The resulting veins grow in a direction parallel to the maximal principal stress and no fracturing is required for vein formation and growth. The simulations show that the two dimensionless ratios t_{def} / t_{dif} and t_{kin} / t_{dif} control the temporal evolution of the dehydration vein length, the fluid pressure and the solid density (Fig. 11). In our simulations both the values of t_{def} and t_{kin} need to be significantly shorter than t_{dif} (Fig. 11). To test the applicability of our simulations to sheared serpentinite at subduction zones, we estimate the value of $t_{dif} = r^2 \eta_f / \left(k \varphi_0^3 K_s \right)$ using the parameter values specified in equation (15) and the initial porosity of 2%. The least constrained parameter in t_{dif} is likely the effective permeability, $k\varphi_0^3$, which in our simulations would be $10^{-22} m^2 \times 0.02^3 = 8 \times 10^{-28} m^2$. Experimental studies suggest that serpentinite permeability decreases exponentially with depth and is in the order of 10^{-23} and 10^{-21} m^2 at a depth of 7 km below seafloor (e.g. Hatakeyama et al., 2017). Using the extrapolation of Hatakeyama et al. (2017) (their equation

1) for their sepertinite termed Sengen-03 provides a permeability of 10^{-30} m^2 for a confining pressure of 9 kbar and 10^{-35} m^2 for a confining pressure of 12.75 kbar, as applied here. Therefore, an effective permeability in the order of 10^{-27} m^2, as used here, seems not unrealistic for serpentinite under a confining pressure of 12.75 kbar and the assumed temperature of 500 °C. For simplicity, we assume here an isotropic permeability, but in natural serpentinite the permeability might be anisotropic. For the considered parameter values we obtain $t_{dif} = 1.25\times10^{11} s \approx 4$ kyr. A representative value of t_{def} in our simulations is $0.05\times t_{dif}$ (Fig. 11A). The inverse of t_{def} corresponds to the applied far-field shearing rate, $\bar{D}_{xy}$, which is then $1.6\times10^{-10} s^{-1}$. A shear strain rate in the order of $10^{-10} s^{-1}$ is feasible for serpentinite shearing at a subduction plate interface (e.g. Chernak and Hirth, 2010). A representative value of t_{kin} in our simulations forming forsterite is $0.001\times t_{dif}$ (Fig. 11D) which corresponds to 4 years. Here, we assume a viscosity of serpentinite of 10^{18} Pas. Despite the importance of serpentinite, its rheology at lithospheric-scale pressure and temperature conditions remains not well constrained (David et al., 2018; Hirauchi et al., 2020, and references therein). However, for the ambient pressure and temperature conditions considered here, viscosities of serpentinite between 10^{17} and 10^{18} Pas seem feasible based on experimental studies (e.g., Chernak and Hirth, 2010; Hilairet et al., 2007). For the applied parameter values, the characteristic time, $t_c = r^2\eta_f / (kK_s)$, is ca. 12 days. The dimensionless simulation times for the ten simulations are between 600 and 1500 (Fig. 11) which then corresponds to a real time between approximately 20 and 50 years, respectively.

We consider here, for simplicity, a fixed chemical composition for which forsterite + water results from dehydration of antigorite + brucite + a negligible amount of free water. We consider this negligle amount of free water simply to be able to calculate thermodynamically the fluid density in the stability field of antigorite + brucite (Fig. 3C). Natural chemical

compositions, in for example the Erro-Tobbio unit, are more complex and feature a higher chemical variability as considered in our model. However, the main aim of our study is to investigate the fundamental coupling between dehydration reactions, fluid flow and rock deformation, justifying the use of a simplified MSH system. Our model suggests that natural areas of serpentinite dehydration, consisting of olivine and water, are mechanically weak due to their high, up to 60%, porosity and water content. After the formation of the dehydration veins, the water eventually escapes the dehydration region, so that finally only olivine is left in the veins.

Field data show that in the Erro Tobbio region the olivine in the veins is metamorphic olivine which resulted from the dehydration of serpentinite. A dehydration origin of the olivine is supported by geochemical studies (e.g., Kempf et al., 2020; Peters et al., 2020). Furthermore, the particular en-échelon orientation of the olivine veins suggest that the vein orientation is controlled by the stress field associated with the serpentinite shearing (Hermann et al. 2000). Therefore, based on published geochemical studies and structural observations we propose that the formation of observed olivine veins was the result of a coupled deformation-reaction process that accelerated the mineral dehydration along particular orientations, controlled by the local stress field in the sheared serpentinite. Similar veins made of metamorphic olivine have been described from subducted serpentinite, such as in the Zermatt-Saas unit in the Central Alps (e.g., Kempf et al., 2020).

The initial distribution of porosity in the presented simulations is simple and defined by a Gaussian distribution. Such a simple initial porosity distribution is again useful to study the fundamental coupling of dehydration reactions and rock deformation. More realistic would likely be an initial random distribution of porosity. To test whether the studied formation of dehydration veins also occurs for a more realistic initial porosity distribution, we performed one simulation with an initial random porosity distribution. The initial values of

569 porosity vary randomly between 2 and 16% in the model domain. We generated the initial
570 porosity distribution with the random field generator presented in Räss et al. (2019). For this
571 simulation, we applied $t_{def} / t_{dif} = 0.012$ and $t_{kin} / t_{dif} = 8.2\times10^{-4}$. Furthermore, the initial
572 values for p and p_f are 12.73 kbar. All other parameters are identical to the values of the
573 first simulation (Fig. 5). The simulation shows that during shearing many dehydration veins
574 with increasing solid density and porosity are formed, similar to the simulations with an initial
575 Gaussian porosity distribution (Fig. 12). Particularly, despite the variability in shape of the
576 dehydrating regions, the longest axis of the dehydrating regions always grows in the direction
577 of the maximum principal stress. Hence, the results with an initial random porosity
578 distribution suggest that the investigated simulations with an initial Gaussian porosity
579 distribution capture the first-order mechanisms of shear-driven dehydration vein formation for
580 more complex and natural model configurations. Furthermore, the simulation shows the
581 formation of many veins with similar length which is similar to observations from natural
582 olivine veins (Fig. 1A to C). The generation of many similar veins results from the self-
583 limiting nature of vein growth (Fig. 11A and D) which prohibits the generation of few large
584 veins.

585 The presented model could potentially be applied to investigate fluid-related processes
586 causing episodic tremor and slow-slip events (ETS; e.g., Peng & Gomberg 2010). Despite the
587 lack of consensus on the inter-relationships between mineral dehydration, fluid flow, critical
588 stress and ETS, the coincidence of the location of low-frequency earthquakes to regions with
589 high Vp/Vs ratios requires the consideration of fluid flow and mineral dehydration in these
590 settings (e.g., Burlini et al. 2009; Kato et al. 2010; Shelly et al. 2006; Van Avendonk et al.,
591 2010). For example, Van Avendonk et al. (2010) infer a zone of very high Vp/Vs ratio of 6 at
592 the top of the subducting Cocos slab between 35 and 55 km depth, lying downdip of the
593 seismogenic zone. They propose that these high Vp/Vs ratios are due to several-meter thick

shear zones under high pore pressure and that the hydrous pore fluids were generated by prograde dehydration reactions. The 35 to 55 km depth range with inferred high Vp/Vs ratios corresponds to the depth range and ambient pressure considered in our model. In addition, the correlation of rapid-tremor migration to pore-pressure waves suggests that this coincidence can be explained by the coupled processes of dehydration, fault weakening and tremor migration (Cruz-Atienz et al. 2018). Thus, the formation of fluid-filled veins, as modelled here, can be correlated to the transient weakening that is inferred in regions of mineral dehydration. Furthermore, the dehydration reaction, generating olivine-fluid bearing veins, and the subsequent fluid escape, leaving behind olivine-only veins, will cause a viscosity inversion: when significant fluid is present in the olivine bearing veins, then the effective viscosity of the olivine-fluid veins is smaller than the viscosity of the serpentinite; but once the fluid has escaped the veins the effective viscosity of the olivine-only veins is larger than the viscosity of the serpentinte. We expect that, under the presence of a general anisotropic stress field, the vein formation will lead to an increase of the anisotropic effective viscosity of the subducted mantle rocks as a result of the different effective viscosities of serpentinite and olivine + fluid assemblages. When the fluid is completely drained from these veins, the viscosity contrast between olivine and serpentinite is such that the associated anisotropy will be permanent.

5. Conclusions

We present a hydro-mechanical-chemical model to investigate the reaction antigorite + brucite = forsterite + water. The model can explain shear-driven formation of dehydration veins in ductile serpentinite and, hence, supports the hypothesis of shear-driven formation of metamorphic olivine veins in the serpentinites of the Erro Tobbio unit (Fig. 1). Vein formation is triggered by fluid pressure perturbations caused by local perturbations of a

porosity-dependent effective viscosity. The veins consist of a weak forsterite-water mixture and grow in a direction parallel to the maximal principal stress which is controlled by the applied far-field simple shearing. The modelled growth of the dehydration veins is not a stable or runaway process but a self-limiting process because the fluid pressure perturbations that drive the vein growth decrease during progressive shearing due to fluid flow.

In our model, three characteristic time scales control the formation of dehydration veins: (1) The time scale of fluid pressure diffusion, t_{dif}, which controls porous fluid flow via Darcy's law, (2) the time scale of the far-field shearing, t_{def}, which is the inverse of the far-field shearing rate and (3) the time scale of the mineral-reaction kinetics, t_{kin}, which controls the time to achieve thermodynamic equilibrium. To form an olivine (here forsterite) vein, the kinetic reaction rate for the transformation from serpentinite to olivine must be fast enough so that olivine can form during vein growth, while significant fluid pressure perturbations exist. The numerical simulations suggest that the kinetic reaction rate should be at least two orders of magnitude faster than the characteristic rate of fluid pressure diffusion.

In our models, the temporal evolution of porosity during dehydration is controlled by three mechanisms: solid volume change, solid density variation and reactive mass transfer. All three mechanisms have a similar impact on the porosity evolution. Hence, our model shows that deformation of the solid rock should be considered when quantifying dehydration vein formation. The fluid pressure distribution is mainly controlled by the total pressure distribution. Mass transfer, porosity variation and solid density variation impact the fluid pressure distribution to a minor extend and only in the dehydrating region.

The presented model can help to understand the formation of olivine veins in serpentinite mylonites in subduction zones. Such veins are observed in several high pressure serpentinites in the Western Alps and Liguria. The modelled veins have a similar orientation as natural en-échelon olivine veins in serpentinite mylonite. The self-limiting feature of the

644 modelled vein growth might also explain the natural observation of many smaller olivine
645 veins and the absence of few large olivine veins. Furthermore, the presented model can
646 explain transient weakening during dehydration in deforming rock which may be an important
647 process during episodic tremor and slow-slip observed in subduction zones.

648

649 **Acknowledgements**

650 S.M.S. is grateful for theoretical advices from Y. Podladchikov and for practical
651 programming help of T. Duretz. This work was supported by the University of Lausanne.
652 E.M. acknowledges the Johannes Gutenberg University of Mainz for financial support. L.R.
653 acknowledges financial support from the Swiss University Conference and the Swiss Council
654 of Federal Institutes of Technology through the Platform for Advanced Scientific Computing
655 (PASC) program, obtained via the PASC project GPU4GEO. There is no conflict of interest.

656

657 **Availability Statement**

658 The software developed and used in the scope of this study is licensed under MIT
659 License. The latest versions of the code is available for download from GitHub at:
660 https://github.com/PTsolvers/PseudoTransientHMC.jl (last access: 18 May 2022). Past and
661 future versions of the software are available from a permanent DOI repository (Zenodo) at:
662 https://doi.org/10.5281/zenodo.6559431 (Schmalholz and Räss, 2022). The codes are written
663 using the Julia programming language and execute on graphical processing units (GPUs).
664 Refer to the repository's README for additional information.

665

666 **Appendix**

667 **A1. Pseudo-transient time steps**

To solve the system of equations (14) iteratively, we apply the following physical, Δt, pseudo-transient (PT), Δt^{PT}, time steps:

$$
\begin{aligned}
\Delta t &= \frac{1}{2}\frac{r^2 \eta_f}{k K_s} \\
\Delta t_{\phi}^{PT} &= \Delta t \\
\Delta t_{pf}^{PT} &= \frac{1}{16.1}\frac{\max\left(\Delta x, \Delta y\right)^2}{\max\left(4\frac{k \phi^3 K_s}{\eta_f}\right)} \\
\Delta t_{v}^{PT} &= \frac{1}{24.15}\frac{\max\left(\Delta x, \Delta y\right)^2}{\max\left(\eta^s\right)} \\
\Delta t_{p}^{PT} &= 471\frac{\max\left(\eta^s\right) dx}{w}
\end{aligned}
\qquad \text{(A1)}
$$

where Δx and Δy are horizontal and vertical numerical grid spacing, respectively. More information concerning the choice of such PT time steps can be found in Wang et al. (2022).

A2. Numerical resolution test

We present here the results of a numerical resolution test. Such test is essential to determine whether the evolution of the dehydrating region is independent of the employed numerical resolution. We performed the first simulation (Fig. 5) with the following different numerical resolutions: 150×150, 300×300, 500×500, 700×700 and 900×900 grid points (Fig. A1). For a dimensionless model time of 950, the ratio of the mean porosity in the model domain divided by the mean porosity for a simulation with 900 × 900 grid points is plotted versus the corresponding resolution for simulations with different resolution (Fig. A1A). Similar ratios are plotted for the minimum fluid pressure in the model domain and the vein length. The higher the resolution, the less the three ratios vary, indicating the convergence of the numerical results upon increasing numerical resolution. The evolution of the minimum

685 fluid pressure in the model domain with time is shown for different numerical resolutions
686 (Fig. A1B). With larger numerical resolution, the temporal evolution of the minimum fluid
687 pressure varies less, indicating again the convergence of the numerical results for increasing
688 numerical resolution. Finally, the spatial distribution of p_f at a dimensionless time of 785 is
689 displayed for three different resolutions (Fig. A1C to E). For a resolution of 150×150 the
690 contours of p_f are jagged, confirming an insufficient numerical resolution (Fig. A1C). For
691 numerical resolutions of 500×500 and 900×900 the contours of p_f are smooth and the
692 colormaps of p_f cannot be distinguished by eye (Fig. A1D and E).The numerical resolution
693 test shows that the applied numerical model provides results which converge for increasing
694 numerical resolution and are, hence, not dependent on the numerical resolution.

References

Aharonov, E., M. Spiegelman, and P. Kelemen (1997), Three-dimensional flow and reaction in porous media: Implications for the Earth's mantle and sedimentary basins, Journal of Geophysical Research-Solid Earth, 102(B7), 14821-14833, doi:10.1029/97jb00996.

Aharonov, E., J. A. Whitehead, P. B. Kelemen, and M. Spiegelman (1995), Channeling instability of upwelling melt in the mantle, Journal of Geophysical Research-Solid Earth, 100(B10), 20433-20450, doi:10.1029/95jb01307.

Audet, P., M. G. Bostock, N. I. Christensen, and S. M. Peacock (2009), Seismic evidence for overpressured subducted oceanic crust and megathrust fault sealing, Nature, 457(7225), 76-78, doi:10.1038/nature07650.

Baltzell, C., E. M. Parmentier, Y. Liang, and S. Tirupathi (2015), A high-order numerical study of reactive dissolution in an upwelling heterogeneous mantle: 2. Effect of shear deformation, Geochemistry Geophysics Geosystems, 16(11), 3855-3869, doi:10.1002/2015gc006038.

Bebout, G. E. (2014), Chemical and Isotopic Cycling in Subduction Zones, in Treatise on Geochemistry, edited by H. D. Holland and K. K. Turekian, pp. 703-747, Elsevier.

Beinlich, A., T. John, J. Vrijmoed, M. Tominaga, T. Magna, and Y. Podladchikov (2020), Instantaneous rock transformations in the deep crust driven by reactive fluid flow, Nature Geoscience, 13(4), 307-311.

Bessat, A., S. Pilet, Y. Y. Podladchikov, and S. M. Schmalholz (2022), Melt Migration and Chemical Differentiation by Reactive Porosity Waves, Geochemistry Geophysics Geosystems, 23(2), doi:10.1029/2021gc009963.

718 Bloch, W., T. John, J. Kummerow, P. Salazar, O. S. Krüger, and S. A. Shapiro (2018),
719 Watching Dehydration: Seismic Indication for Transient Fluid Pathways in the Oceanic
720 Mantle of the Subducting Nazca Slab, Geochemistry, Geophysics, Geosystems, 19(9), 3189-
721 3207, doi:https://doi.org/10.1029/2018GC007703.

722 Brantut, N., J. Sulem, and A. Schubnel (2011), Effect of dehydration reactions on earthquake
723 nucleation: Stable sliding, slow transients, and unstable slip, Journal of Geophysical
724 Research: Solid Earth, 116(B5).

725 Burlini, L., G. Di Toro, and P. Meredith (2009), Seismic tremor in subduction zones: Rock
726 physics evidence, Geophysical Research Letters, 36, doi:10.1029/2009gl037735.

727 Chernak, L. J., and G. Hirth (2010), Deformation of antigorite serpentinite at high temperature
728 and pressure, Earth and Planetary Science Letters, 296(1-2), 23-33,
729 doi:10.1016/j.epsl.2010.04.035.

730 Connolly, J. (1997), Devolatilization-generated fluid pressure and deformation-propagated
731 fluid flow during prograde regional metamorphism, Journal of Geophysical Research: Solid
732 Earth, 102(B8), 18149-18173.

733 Connolly, J. (2005), Computation of phase equilibria by linear programming: a tool for
734 geodynamic modeling and its application to subduction zone decarbonation, Earth and
735 Planetary Science Letters, 236(1-2), 524-541.

736 Connolly, J. (2009), The geodynamic equation of state: What and how, Geochemistry
737 Geophysics Geosystems, 10, doi:10.1029/2009gc002540.

738 Cruz-Atienza, V. M., C. Villafuerte, and H. S. Bhat (2018), Rapid tremor migration and pore-
739 pressure waves in subduction zones, Nature Communications, 9(1), 2900,
740 doi:10.1038/s41467-018-05150-3.

741 David, E. C., N. Brantut, L. N. Hansen, and T. M. Mitchell (2018), Absence of Stress-Induced
742 Anisotropy During Brittle Deformation in Antigorite Serpentinite, Journal of Geophysical
743 Research-Solid Earth, 123(12), 10616-10644, doi:10.1029/2018jb016255.

744 Evans, O., M. Spiegelman, and P. B. Kelemen (2020), Phase-Field Modeling of Reaction-
745 Driven Cracking: Determining Conditions for Extensive Olivine Serpentinization, Journal of
746 Geophysical Research: Solid Earth, 125(1), e2019JB018614.

747 Fowler, A. C. (1985), A mathematical model of magma transport in the asthenosphere,
748 Geophysical & Astrophysical Fluid Dynamics, 33(1-4), 63-96,
749 doi:10.1080/03091928508245423.

750 Frank, W. B., N. M. Shapiro, A. L. Husker, V. Kostoglodov, H. S. Bhat, and M. Carnpillo
751 (2015), Along-fault pore-pressure evolution during a slow-slip event in Guerrero, Mexico,
752 Earth and Planetary Science Letters, 413, 135-143, doi:10.1016/j.epsl.2014.12.051.

753 Gerya, T. (2019), Introduction to numerical geodynamic modelling, Cambridge University
754 Press.

755 Gomberg, J., Cascadia, and B. W. Group (2010), Slow-slip phenomena in Cascadia from
756 2007 and beyond: A review, Bulletin, 122(7-8), 963-978.

757 Hacker, B. R., S. M. Peacock, G. A. Abers, and S. D. Holloway (2003), Subduction factory 2.
758 Are intermediate-depth earthquakes in subducting slabs linked to metamorphic dehydration
759 reactions?, Journal of Geophysical Research: Solid Earth, 108(B1).

760 Hatakeyama, K., I. Katayama, K.-i. Hirauchi, and K. Michibayashi (2017), Mantle hydration
761 along outer-rise faults inferred from serpentinite permeability, Scientific Reports, 7(1), 13870,
762 doi:10.1038/s41598-017-14309-9.

763 Hebert, L. B., P. Antoshechkina, P. Asimow, and M. Gurnis (2009), Emergence of a low-
764 viscosity channel in subduction zones through the coupling of mantle flow and
765 thermodynamics, Earth and Planetary Science Letters, 278(3-4), 243-256,
766 doi:10.1016/j.epsl.2008.12.013.

767 Hermann, J., O. Müntener, and M. Scambelluri (2000), The importance of serpentinite
768 mylonites for subduction and exhumation of oceanic crust, Tectonophysics, 327(3-4), 225-
769 238.

770 Hilairet, N., B. Reynard, Y. B. Wang, I. Daniel, S. Merkel, N. Nishiyama, and S. Petitgirard
771 (2007), High-pressure creep of serpentine, interseismic deformation, and initiation of
772 subduction, Science, 318(5858), 1910-1913, doi:10.1126/science.1148494.

773 Hirauchi, K., I. Katayama, and Y. Kouketsu (2020), Semi-brittle deformation of antigorite
774 serpentinite under forearc mantle wedge conditions, Journal of Structural Geology, 140,
775 doi:10.1016/j.jsg.2020.104151.

776 Holland, T., and R. Powell (1998), An internally consistent thermodynamic data set for
777 phases of petrological interest, Journal of metamorphic Geology, 16(3), 309-343.

778 Huber, K., J. C. Vrijmoed, and T. John (2022), Formation of Olivine Veins by Reactive Fluid
779 Flow in a Dehydrating Serpentinite, Geochemistry, Geophysics, Geosystems, 23(6),
780 e2021GC010267, doi:https://doi.org/10.1029/2021GC010267.

781 John, T., N. Gussone, Y. Y. Podladchikov, G. E. Bebout, R. Dohmen, R. Halama, R. Klemd,
782 T. Magna, and H. M. Seitz (2012), Volcanic arcs fed by rapid pulsed fluid flow through
783 subducting slabs, Nature Geoscience, 5(7), 489-492, doi:10.1038/ngeo1482.

784 Kato, A., et al. (2010), Variations of fluid pressure within the subducting oceanic crust and
785 slow earthquakes, Geophysical Research Letters, 37, doi:10.1029/2010gl043723.

786 Kempf, E. D., J. Hermann, E. Reusser, L. P. Baumgartner, and P. Lanari (2020), The role of
787 the antigorite + brucite to olivine reaction in subducted serpentinites (Zermatt, Switzerland)
788 (vol 113, 16, 2020), Swiss Journal of Geosciences, 113(1), doi:10.1186/s00015-020-00377-z.

789 Kolditz, O., H. Shao, W. Wang, and S. Bauer (2016), Thermo-hydro-mechanical chemical
790 processes in fractured porous media: modelling and benchmarking, 313 pp., Springer,
791 doi:10.1007/978-3-319-11894-9.

792 Labrousse, L., G. Hetenyi, H. Raimbourg, L. Jolivet, and T. B. Andersen (2010), Initiation of
793 crustal-scale thrusts triggered by metamorphic reactions at depth: Insights from a comparison
794 between the Himalayas and Scandinavian Caledonides, Tectonics, 29,
795 doi:10.1029/2009tc002602.

796 Llana-Fúnez, S., J. Wheeler, and D. R. Faulkner (2012), Metamorphic reaction rate controlled
797 by fluid pressure not confining pressure: implications of dehydration experiments with
798 gypsum, Contributions to Mineralogy and Petrology, 164(1), 69-79, doi:10.1007/s00410-012-
799 0726-8.

800 Malvoisin, B., Y. Y. Podladchikov, and A. V. Myasnikov (2021), Achieving complete
801 reaction while the solid volume increases: Anumerical model applied to serpentinisation,
802 Earth and Planetary Science Letters, 563, doi:10.1016/j.epsl.2021.116859.

803 Matter, J. M., and P. B. Kelemen (2009), Permanent storage of carbon dioxide in geological
804 reservoirs by mineral carbonation, Nature Geoscience, 2(12), 837-841, doi:10.1038/ngeo683.

805 McKenzie, D. (1984), The generation and compaction of partially molten rock, J. Petrology,
806 25, 713-765.

807 Moulas, E., S. M. Schmalholz, Y. Podladchikov, L. Tajčmanová, D. Kostopoulos, and L.
808 Baumgartner (2019), Relation between mean stress, thermodynamic, and lithostatic pressure,
809 Journal of metamorphic geology, 37(1), 1-14.

810 Omlin, S., B. Malvoisin, and Y. Y. Podladchikov (2017), Pore fluid extraction by reactive
811 solitary waves in 3-D, Geophysical Research Letters, 44(18), 9267-9275.

812 Pandey, S. N., V. Vishal, and A. Chaudhuri (2018), Geothermal reservoir modeling in a
813 coupled thermo-hydro-mechanical-chemical approach: A review, Earth-Science Reviews,
814 185, 1157-1169, doi:10.1016/j.earscirev.2018.09.004.

815 Peacock, S. M. (1990), Fluid processes in subduction zones, Science, 248(4953), 329-337,
816 doi:10.1126/science.248.4953.329.

817 Peng, Z. G., and J. Gomberg (2010), An integrated perspective of the continuum between
818 earthquakes and slow-slip phenomena, Nature Geoscience, 3(9), 599-607,
819 doi:10.1038/ngeo940.

820 Peters, D., T. Pettke, T. John, and M. Scambelluri (2020), The role of brucite in water and
821 element cycling during serpentinite subduction – Insights from Erro Tobbio (Liguria, Italy),
822 Lithos, 360-361, 105431, doi:https://doi.org/10.1016/j.lithos.2020.105431.

823 Pettke, T., and A. Bretscher (2022), Fluid-mediated element cycling in subducted oceanic
824 lithosphere: The orogenic serpentinite perspective, Earth-Science Reviews, 225,
825 doi:10.1016/j.earscirev.2021.103896.

826 Plümper, O., T. John, Y. Y. Podladchikov, J. C. Vrijmoed, and M. Scambelluri (2017), Fluid
827 escape from subduction zones controlled by channel-forming reactive porosity, Nature
828 Geoscience, 10(2), 150-156.

829 Poulet, T., A. Karrech, K. Regenauer-Lieb, L. Fisher, and P. Schaubs (2012), Thermal–
830 hydraulic–mechanical–chemical coupling with damage mechanics using ESCRIPTRT and
831 ABAQUS, Tectonophysics, 526, 124-132.

832 Poulet, T., M. Veveakis, M. Herwegh, T. Buckingham, and K. Regenauer-Lieb (2014),
833 Modeling episodic fluid-release events in the ductile carbonates of the Glarus thrust,
834 Geophysical Research Letters, 41(20), 7121-7128, doi:10.1002/2014gl061715.

835 Rass, L., D. Kolyukhin, and A. Minakov (2019), Efficient parallel random field generator for
836 large 3-D geophysical problems, Computers & Geosciences, 131, 158-169,
837 doi:10.1016/j.cageo.2019.06.007.

838 Reiner, M. (1964), The Deborah number, Physics Today, 17(1), 62.

839 Rupke, L. H., J. P. Morgan, M. Hort, and J. A. D. Connolly (2004), Serpentine and the
840 subduction zone water cycle, Earth and Planetary Science Letters, 223(1-2), 17-34,
841 doi:10.1016/j.epsl.2004.04.018.

842 Scambelluri, M., J. Fiebig, N. Malaspina, O. Muntener, and T. Pettke (2004), Serpentinite
843 subduction: Implications for fluid processes and trace-element recycling, International
844 Geology Review, 46(7), 595-613, doi:10.2747/0020-6814.46.7.595.

845 Scambelluri, M., O. Muntener, J. Hermann, G. B. Piccardo, and V. Trommsdorff (1995),
846 Subduction of water into the mantle - history of an Alpine peridotite, Geology, 23(5), 459-
847 462, doi:10.1130/0091-7613(1995)023<0459:Sowitm>2.3.Co;2.

848 Scambelluri, M., E. H. H. Strating, G. B. Piccardo, R. L. M. Vissers, and E. Rampone (1991),
849 Alpine olivine-bearing and titanium clinohumite-bearing assemblages in the Erro Tobbio
850 peridotite (Voltri-massif, NW Italy), Journal of Metamorphic Geology, 9(1), 79-91,
851 doi:10.1111/j.1525-1314.1991.tb00505.x.

852 Schiemenz, A., Y. Liang, and E. M. Parmentier (2011), A high-order numerical study of
853 reactive dissolution in an upwelling heterogeneous mantle-I. Channelization, channel
854 lithology and channel geometry, Geophysical Journal International, 186(2), 641-664,
855 doi:10.1111/j.1365-246X.2011.05065.x.

856 Schmalholz, S. M., E. Moulas, O. Plumper, A. V. Myasnikov, and Y. Y. Podladchikov
857 (2020), 2D Hydro-Mechanical-Chemical Modeling of (De)hydration Reactions in Deforming
858 Heterogeneous Rock: The Periclase-Brucite Model Reaction, Geochemistry Geophysics
859 Geosystems, 21(11), doi:10.1029/2020gc009351.

860 Schmalholz, S. M., and L. Räss (2022), PTsolvers/PseudoTransientHMC.jl:
861 PseudoTransientHMC.jl 0.1.0 (v0.1.0), edited, Zenodo,
862 doi:https://doi.org/10.5281/zenodo.6559431.

863 Schmeling, H., J. P. Kruse, and G. Richard (2012), Effective shear and bulk viscosity of
864 partially molten rock based on elastic moduli theory of a fluid filled poroelastic medium,
865 Geophysical Journal International, 190(3), 1571-1578, doi:10.1111/j.1365-
866 246X.2012.05596.x.

867 Shelly, D. R., G. C. Beroza, and S. Ide (2007), Non-volcanic tremor and low-frequency
868 earthquake swarms, Nature, 446(7133), 305-307.

869 Spitz, R., S. M. Schmalholz, B. J. Kaus, and A. A. Popov (2020), Quantification and
870 visualization of finite strain in 3D viscous numerical models of folding and overthrusting,
871 Journal of Structural Geology, 131, 103945.

872 Sulem, J., and V. Famin (2009), Thermal decomposition of carbonates in fault zones: Slip-
873 weakening and temperature-limiting effects, Journal of Geophysical Research: Solid Earth,
874 114(B3).

875 Taetz, S., T. John, M. Brocker, C. Spandler, and A. Stracke (2018), Fast intraslab fluid-flow
876 events linked to pulses of high pore fluid pressure at the subducted plate interface, Earth and
877 Planetary Science Letters, 482, 33-43, doi:10.1016/j.epsl.2017.10.044.

878 Tarling, M. S., S. A. F. Smith, and J. M. Scott (2019), Fluid overpressure from chemical
879 reactions in serpentinite within the source region of deep episodic tremor, Nature Geoscience,
880 12(12), 1034-1042, doi:10.1038/s41561-019-0470-z.

881 Ulmer, P., and V. Trommsdorff (1995), Serpentine Stability to Mantle Depths and
882 Subduction-Related Magmatism, Science, 268(5212), 858-861,
883 doi:doi:10.1126/science.268.5212.858.

884 Van Avendonk, H. J. A., W. S. Holbrook, D. Lizarralde, M. M. Mora, S. Harder, A. D.
885 Bullock, G. E. Alvarado, and C. J. Ramirez (2010), Seismic evidence for fluids in fault zones
886 on top of the subducting Cocos Plate beneath Costa Rica, Geophysical Journal International,
887 181(2), 997-1016, doi:10.1111/j.1365-246X.2010.04552.x.

888 Wang, L. H., V. M. Yarushina, Y. Alkhimenkov, and Y. Podladchikov (2021), Physics-
889 inspired pseudo-transient method and its application in modelling focused fluid flow with
890 geological complexity, Geophysical Journal International, 229(1), 1-20,
891 doi:10.1093/gji/ggab426.

892 Yarushina, V. M., and Y. Y. Podladchikov (2015), (De) compaction of porous
893 viscoelastoplastic media: Model formulation, Journal of Geophysical Research: Solid Earth,
894 120(6), 4146-4170.

895 **Figures with captions**

896

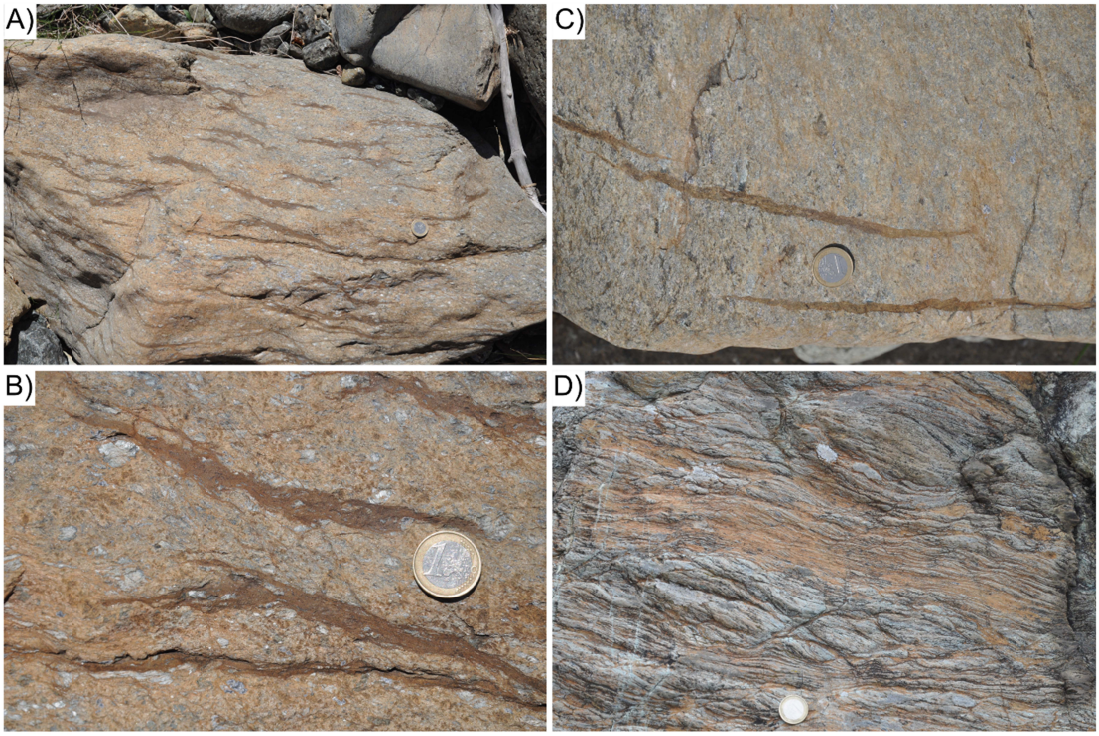

897

898 Figure 1. Natural examples of metamorphic olivine veins in antigorite serpentinite from the
899 Erro Tobbio ultramafic rocks, Ligurian Alps, Italy. A) Overview on the limited spatial extent
900 of olivine bearing veins (with darker color) in weakly deformed serpentinized peridotite. Coin
901 diameter is 2.4 cm. B) Olivine veins with characteristic spacing and aspect ratios in
902 serpentinised peridotite. Detail of picture in A). C) olivine-bearing veins in a serpentinised
903 peridotite, foliation is sub vertical, extent of veins is ca. 20 cm. D) Serpentinite mylonite with
904 different generations of olivine veins. An earlier set is subparallel to the foliation, younger
905 shear bands dissect serpentinite mylonite and olivine veins. Top-to-the-left shear sense. Note
906 the late stage serpentine veins perpendicular to the foliation.

907

908

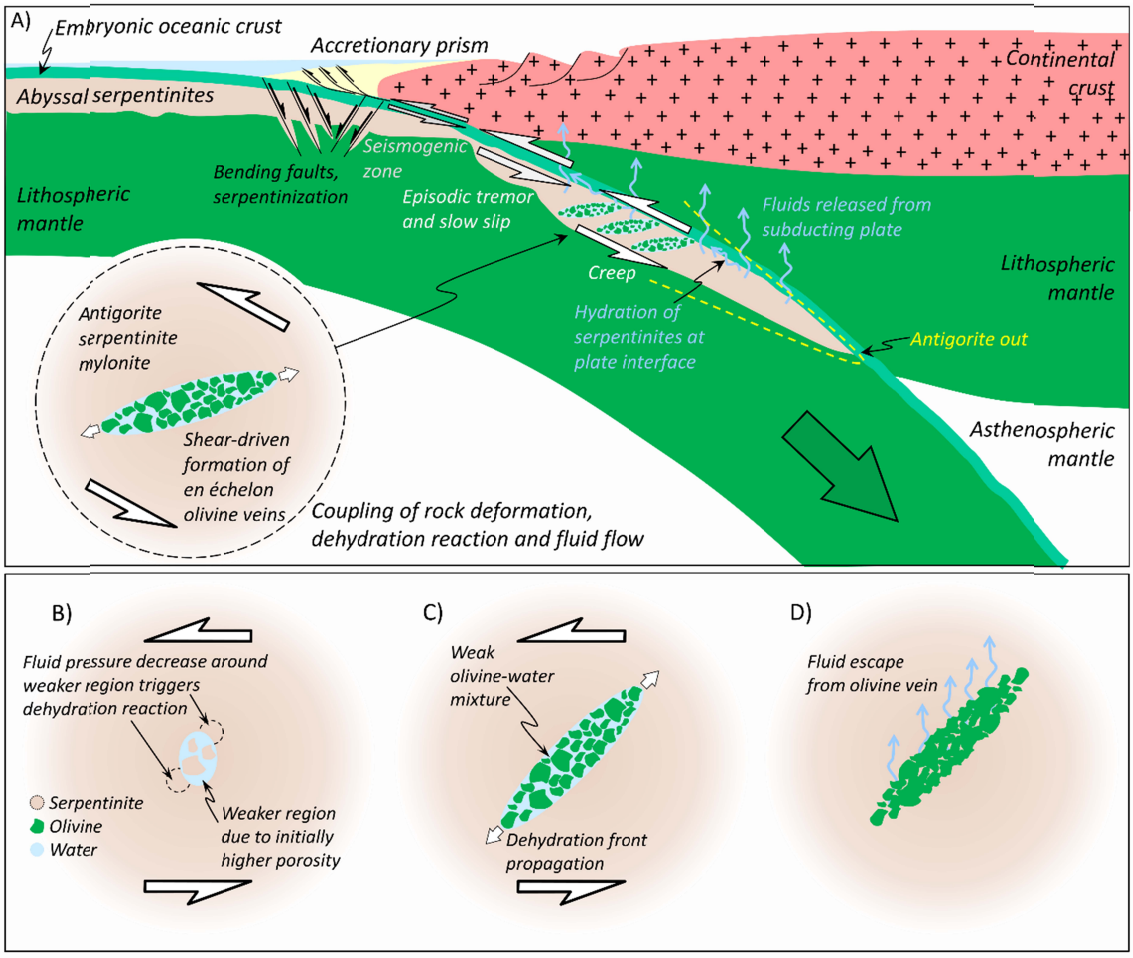

909

910 Figure 2. Simple sketches illustrating the geodynamic setting (A) and the hypothesis for
911 shear-driven dehydration and olivine vein formation in viscous serpentinite (B to D; see text
912 for details).

913

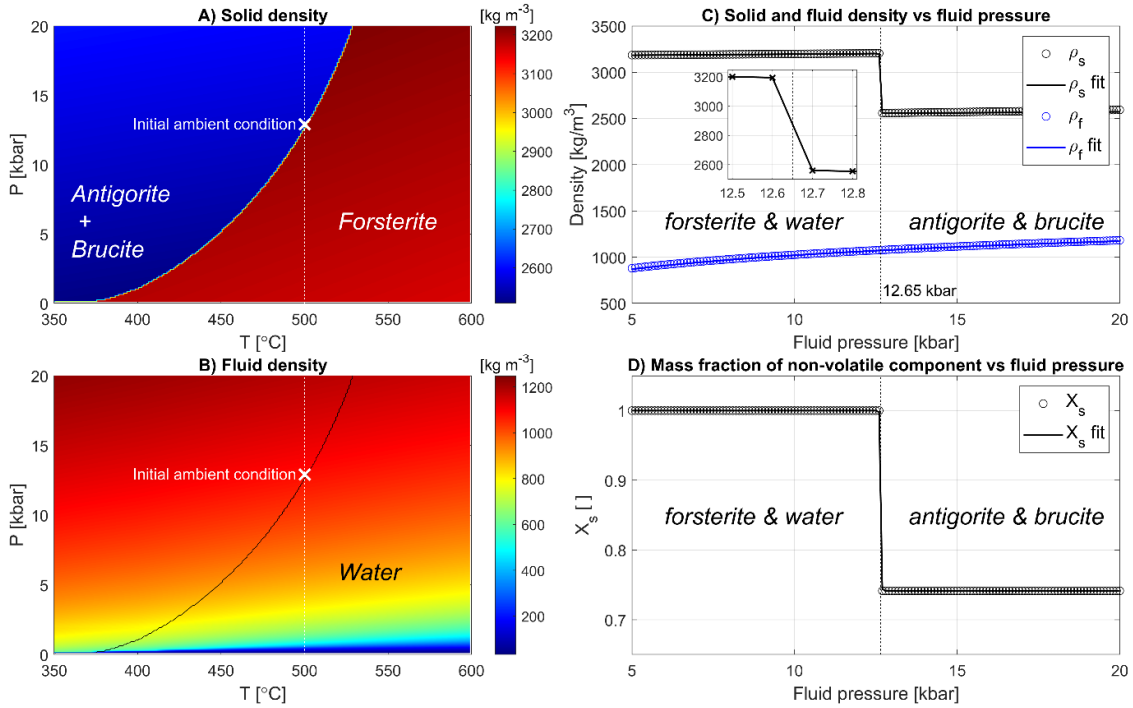

Figure 3. Thermodynamic results obtained from Gibbs' free energy minimization for the system antigorite + brucite = forsterite + water (see text for exact chemical formulas). Density fields of solid (A) and fluid (B) in thermodynamic pressure, P, and temperature, T, space. Corresponding profiles of solid and fluid densities (C) and mass fraction of MgO (D) as a function of fluid pressure at 500 °C. The circles in the three profiles in panels C) and D) are the results from Gibbs energy minimization and the corresponding solid lines are analytical approximations of these profiles (equation (16)), which are used in the numerical algorithm.

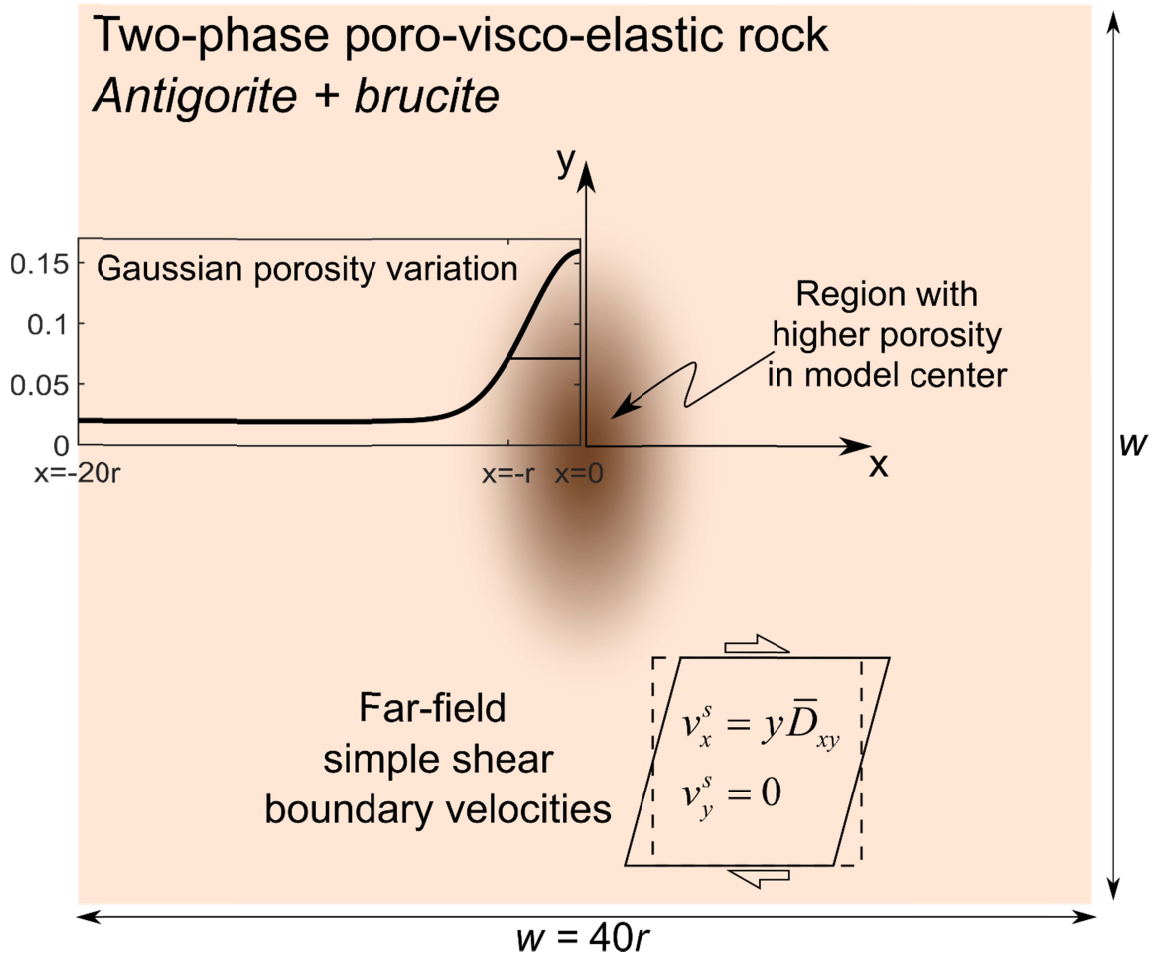

924

925 Figure 4. Sketch of the model configuration and the applied far-field simple shear (bottom
926 right sketch; see text for details). The intitial distribution of the porosity is described by a 2D
927 Gaussian distribution, having an initial horizontal bandwidth of $2r$ (graph in left middle of
928 the sketch) and a vertical bandwidth of $4r$. The width and height of the model is $40r$ and the
929 applied far-field shearing rate is $\bar{D}_{xy}$.

930

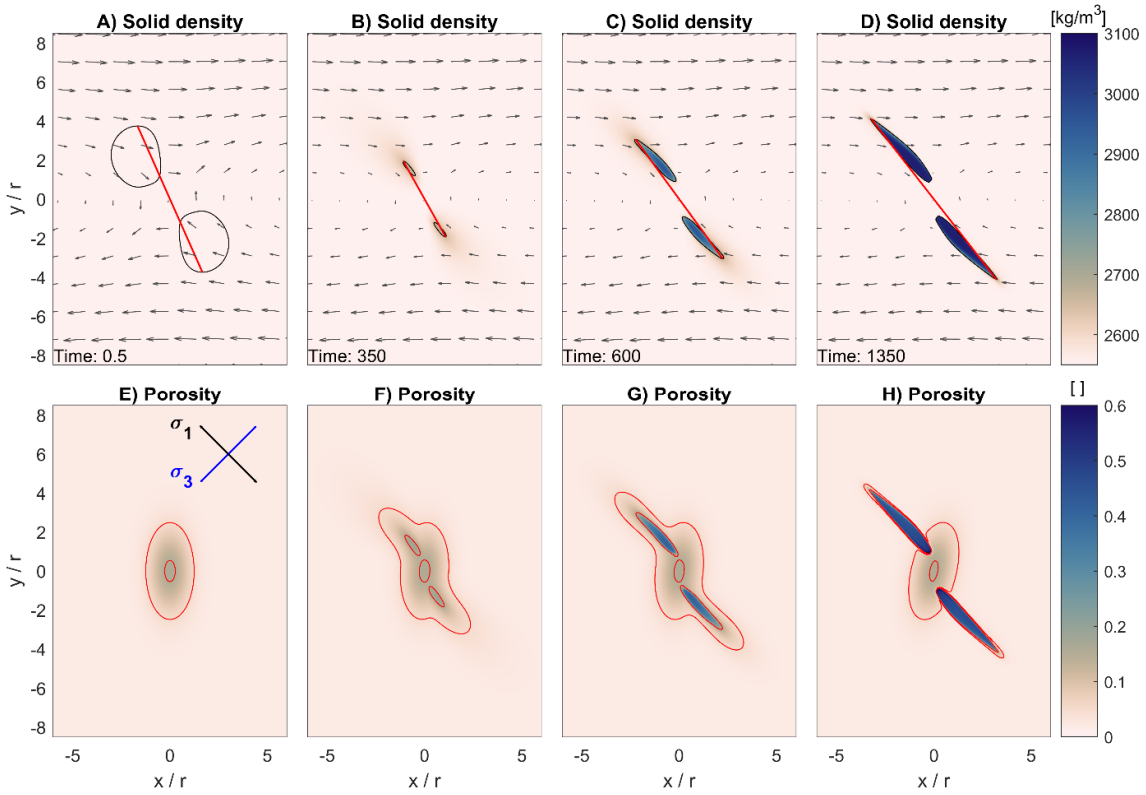

931

932 Figure 5. Representative evolution of a dehydration vein under simple shear for a simulation
933 with $t_{def} / t_{dif} = 0.071$ and $t_{kin} / t_{dif} = 0.0025$. Panels A) to D) show snapshots of solid density
934 for four stages of the simulation, indicated by a dimensionless time (see text). The black
935 contour lines in panels A) to D) indicated the contour for $p_f = 12.65$ kbar (p_f is smaller
936 inside the contour), which is the thermodynamic pressure at the dehydration reaction (see Fig.
937 3). Grey arrows indicate the solid velocities which are dominated by the applied simple shear.
938 The red line connects the highest with the lowest point of the fluid pressure contours and the
939 length of the red line is used as proxy to monitor the vein growth with time. Panels E) to H)
940 show the porosity corresponding to the model times of panels A) to D). In panel E), the black
941 line indicates the direction of the maximal principal stress, σ_1, and the blue line indicates the
942 direction of the minimal principal stress, σ_3, at the location of the intersection of the two
943 lines. The red contours indicate a porosity of 5% (outer contour) and 15% (inner contour).

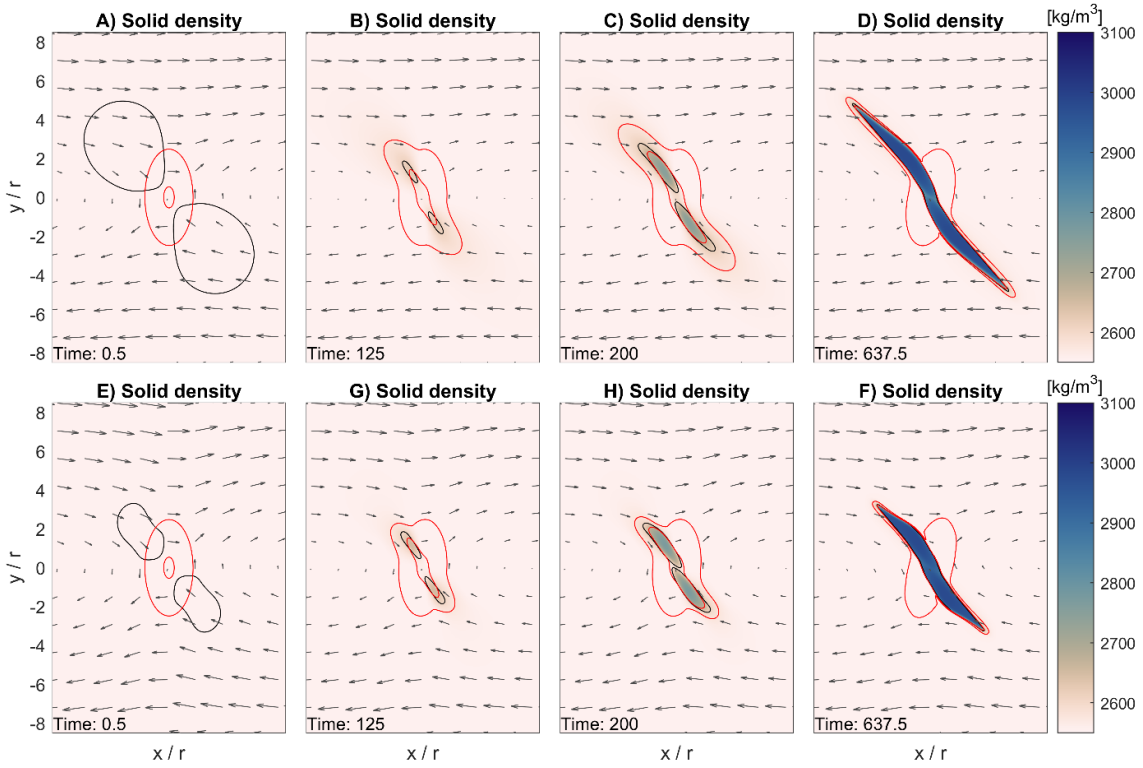

Figure 6. Representative evolution of dehydration veins under simple shear for two simulations with $t_{def} / t_{dif} = 0.038$ and $t_{kin} / t_{dif} = 0.0025$. Colomaps indicate the solid density. The simulation shown in panels A) to D) is purely viscous whereas for the simulation shown in E) to F) a von Mises yield stress of 150 MPa was applied and deformation is visco-plastic. In all panels, the black contour lines indicate the contour for $p_f = 12.65$ kbar (p_f is smaller inside the contour), the grey arrows indicate the solid velocities and the red contours indicate a porosity of 5% (outer contour) and 15% (inner contour).

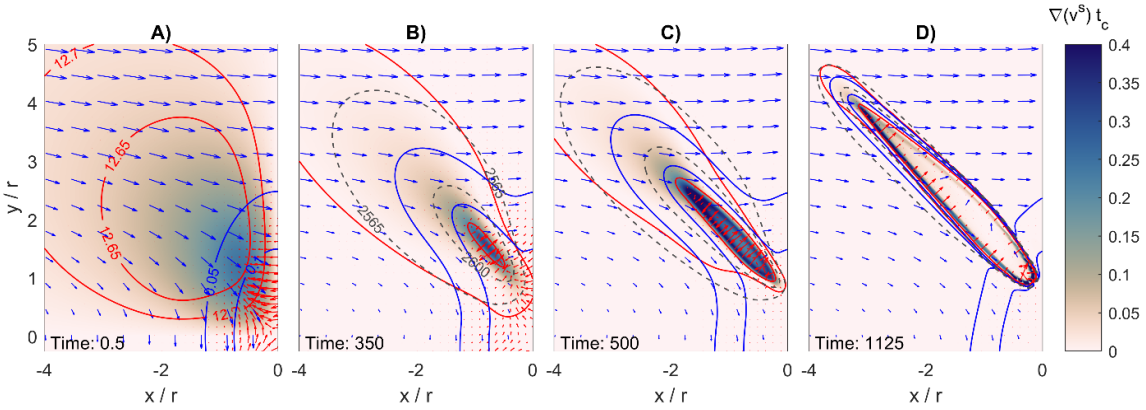

954

955 Figure 7. Evolution of a dehydration vein under simple shear for a simulation (shown in Fig.

956 5) with $t_{def} / t_{dif} = 0.071$ and $t_{kin} / t_{dif} = 0.0025$ at four dimensionless times (see text). The

957 colormaps show the dimensionless divergence of the solid velocity, the red arrows show the

958 fluid velocity field and the blue arrows show the solid velocity field. The two red contours

959 indicate $p_f = 12.65$ (always the inner contour) and 12.7 kbar. The two blue contours indicate

960 a porosity of 5% (outer contour) and 10% (inner contour). The two dashed grey contours

961 indicate a solid density of 2565 kg/m^3 (outer contour) and 2600 kg/m^3 (inner contour). There

962 are no solid density contours in panel A) because all densities are < 2565 kg/m^3.

963

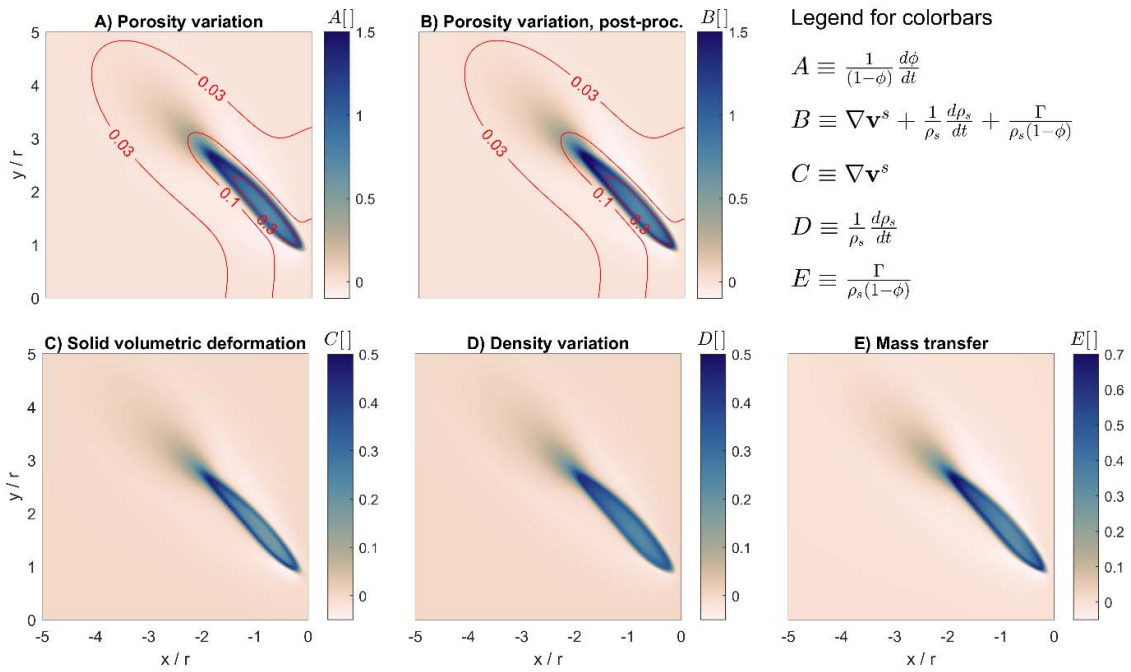

964

965 Figure 8. The three mechanisms (solid volumetric deformation, C, solid-density variation, D,
966 and mass transfer, E) that control the temporal porosity variation (see equation (18)) for a
967 simulation (shown in Fig. 5) with $t_{def} / t_{dif} = 0.071$ and $t_{kin} / t_{dif} = 0.0025$ at a dimensionless
968 time of 550. A) shows the colormap of the term displayed in the legend for A, B) shows the
969 colormap of the term displayed in the legend for B, C) shows the colormap of the term
970 displayed in the legend for C, D) shows the colormap of the term displayed in the legend for
971 D and E) shows the colormap of the term displayed in the legend for E. All displayed terms
972 represent dimensionless rates which can be made dimensionless by multiplying with the
973 characteristic time, t_c (see text).

974

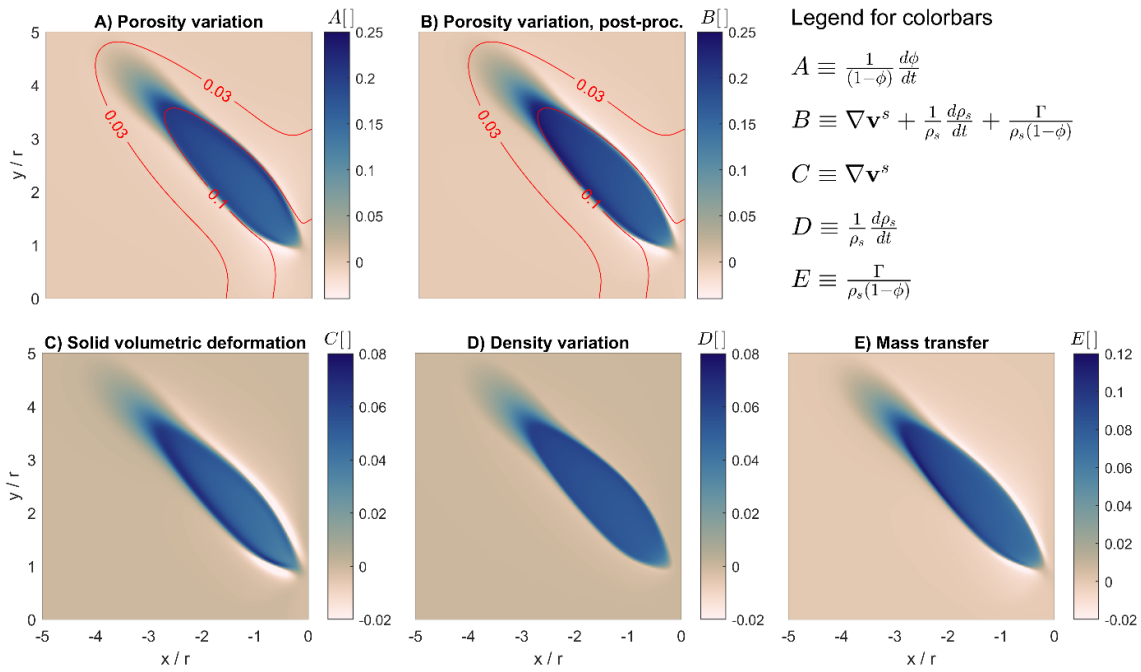

975

976 Figure 9. The three mechanisms (solid volumetric deformation, C, solid-density variation, D,
977 and mass transfer, E) that control temporal porosity variation (see equation (18)) for a
978 simulation with $t_{def} / t_{dif} = 0.071$ and $t_{kin} / t_{dif} = 0.022$ at a dimensionless time of 800. A)
979 shows the colormap of the term displayed in the legend for A, B) shows the colormap of the
980 term displayed in the legend for B, C) shows the colormap of the term displayed in the legend
981 for C, D) shows the colormap of the term displayed in the legend for D and E) shows the
982 colormap of the term displayed in the legend for E. All displayed terms represent
983 dimensionless rates which can be made dimensionless by multiplying with the characteristic
984 time, t_c (see text).

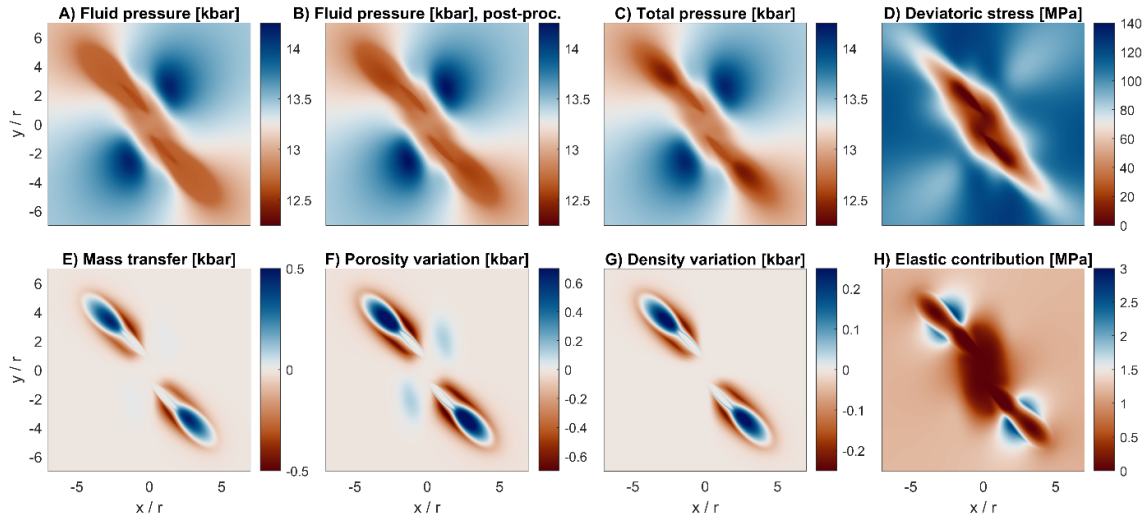

Figure 10. The five mechanisms and quantities that control the distribution of fluid pressure (equation (19)) for a simulation (shown in Fig. 5) with $t_{def} / t_{dif} = 0.071$ and $t_{kin} / t_{dif} = 0.0025$ at a dimensionless time of 550. A) Colormap of fluid pressure which was calculated by the numerical simulation and B) fluid pressure which was post-processed from numerical results using equation (19). C) shows the total pressure and D) the deviatoric stress, τ_{II}, which was calculated by the numerical simulation. E) shows the contribution to the fluid pressure due to mass transfer (last term on right-hand side of equation (19)), F) due to porosity variation (third term on right-hand side of equation (19)), G) due to solid density variation (fourth term on right-hand side of equation (19)) and H) due to elastic deformation (second term on right-hand side of equation (19)). All quantities displayed in E) to H) have been post-processed from numerical results.

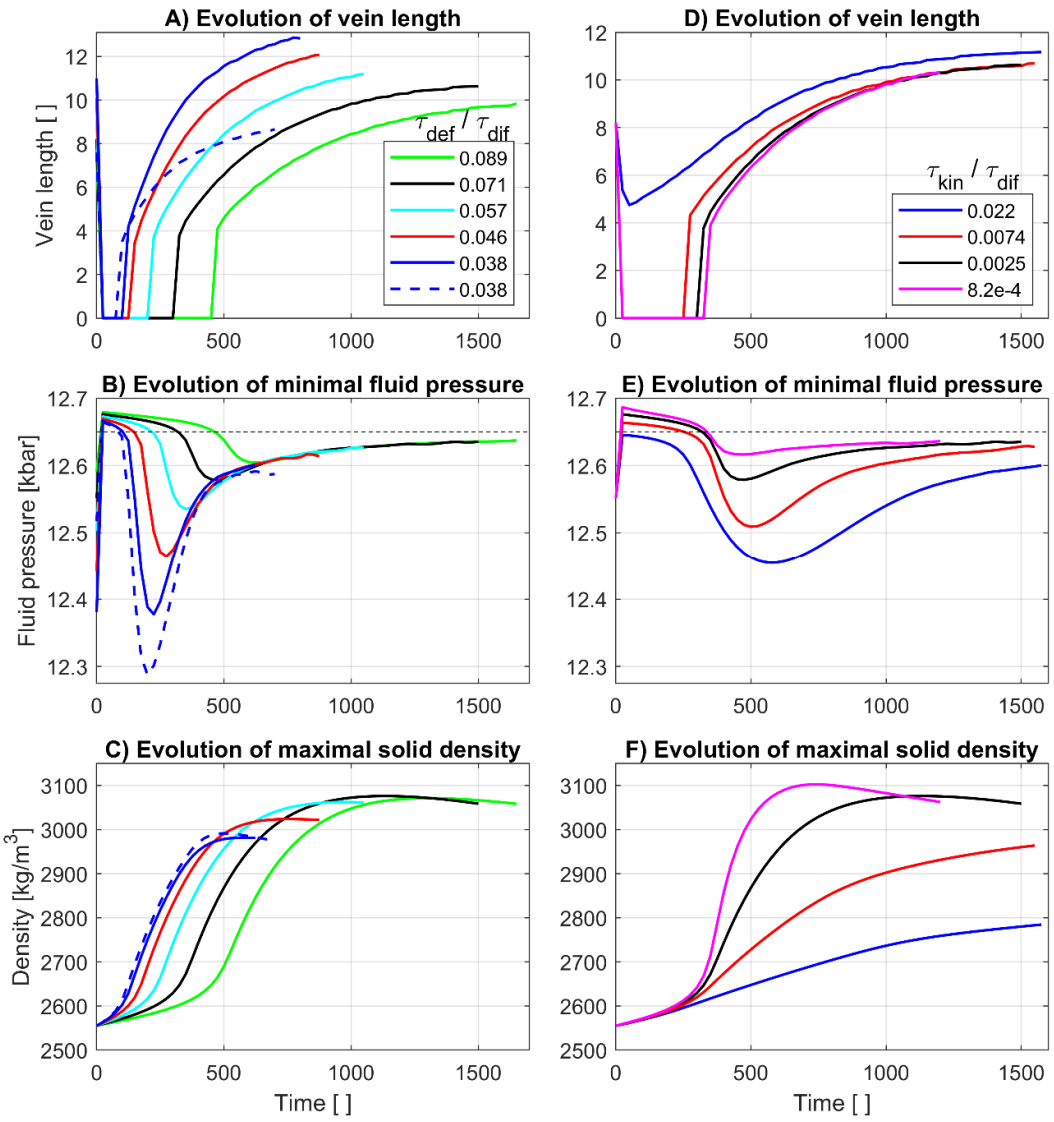

999

1000 Figure 11. Impact of far-field shearing rate (A to C) and kinetic reaction rate (B to F) on the
1001 evolution of vein length (A and D), on the minimal value of the fluid pressure in the model
1002 domain (B and E) and on the evolution of the maximal solid density in the model domain (C
1003 and F). For the results displayed in panels A) to C) the ratio $t_{kin} / t_{dif} = 0.0025$ for all
1004 simulations. For the results displayed in panels D) to F) the ratio $t_{def} / t_{dif} = 0.071$ for all
1005 simulations. Results indicated with the dashed blue line are obtained by the same simulation
1006 which provided results indicated by the solid blue line, but with a von Mises yield stress of
1007 150 MPa (results of the two simulations are also displayed in Fig. 6).

1008

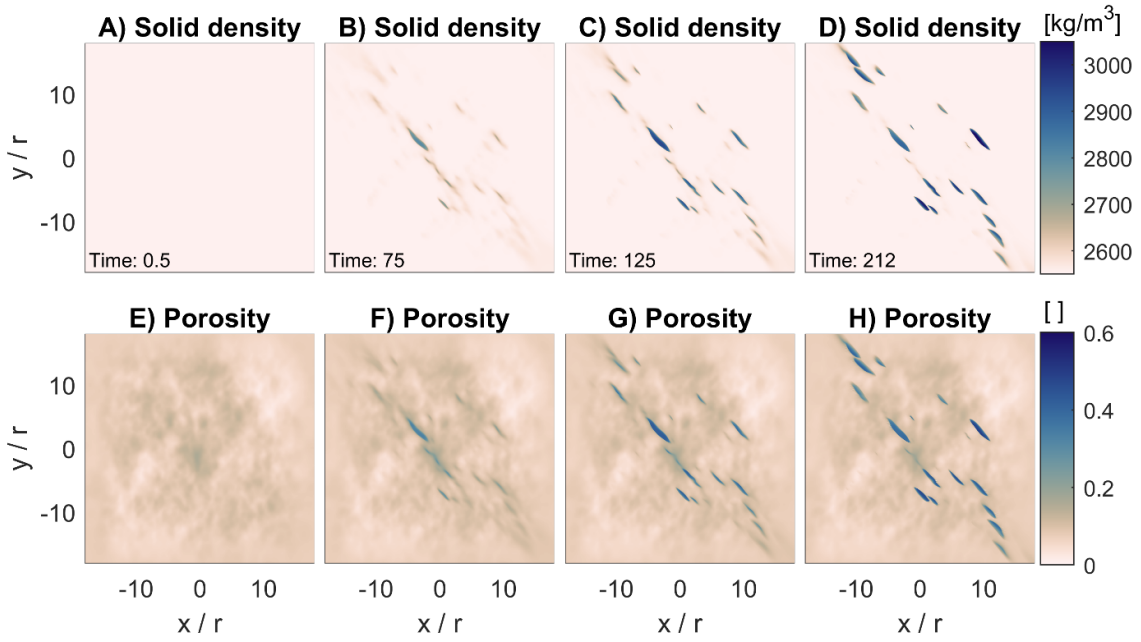

1009

1010 Figure 12. Evolution of solid density (A to D) and corresponding porosity (E to H) for a

1011 simulation with an initial random distribution of porosity (see Discussion).

1012

1013

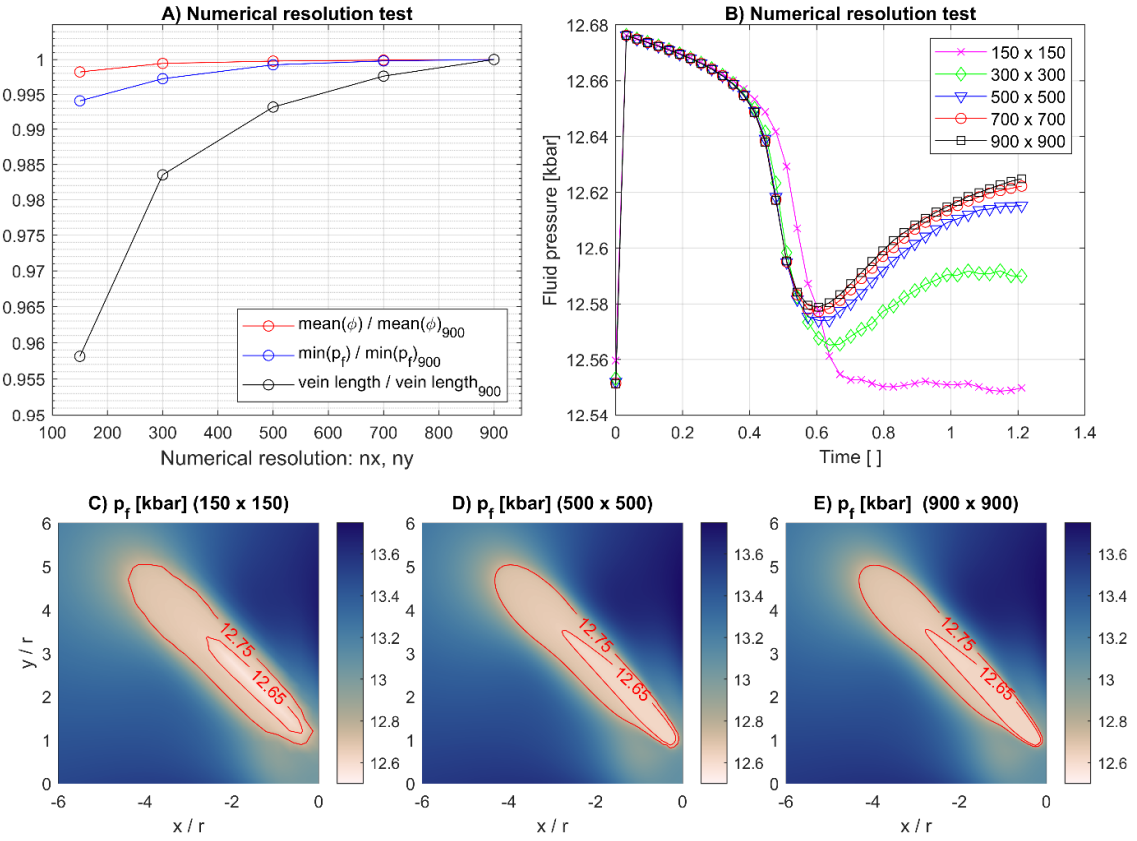

Figure A1. Numerical resolution test for the simulation with $t_{def} / t_{dif} = 0.071$ and $t_{kin} / t_{dif} = 0.0025$ (see Fig. 5). A) For a dimensionless model time of 1.21, the ratio of the mean porosity in the model domain divided by the mean porosity for a simulation with a resolution of 900 × 900 grid points is plotted versus the corresponding resolution for simulations with different resolution. Similar ratios are plotted for the minimum fluid pressure in the model domain and the vein length. The larger the resolution, the less the three ratios vary. B) Evolution of minimum fluid pressure in the model domain with time for different numerical resolutions (see legend). With larger resolution, the evolution of fluid pressure varies less. C) to D) At a dimensionless model time of 1.0, the colormap of the fluid pressure is displayed for three different resolutions (see numbers in panel titles). Two contour lines of fluid pressure are displayed for better comparability.

1027

1028 Table 1. Model variables and parameters.

Symbol	Name / Definition	Units
t_{kin}	Kinetic time scale	$[s]$
t_{dif}	$= r^2 \eta_f / \left(k \varphi_0^3 K_s \right)$	$[s]$
t_{def}	$= 1 / \bar{D}_{xx}$	$[s]$
p_f	Fluid pressure	$[Pa]$
φ	Porosity	$[\ ]$
φ_0	Initial porosity	$[\ ]$
ρ_s	Solid density	$\left[kg \cdot m^{-3} \right]$
ρ_f	Fluid density	$\left[kg \cdot m^{-3} \right]$
X_s	Mass fraction MgO	$[\ ]$
p	Total pressure	$[Pa]$
v_x^s , v_y^s	Solid velocities	$\left[m \cdot s^{-1} \right]$
v_x^f , v_y^f	Fluid velocities	$\left[m \cdot s^{-1} \right]$
$\left\| \mathbf{v}^f \right\|$	$= \sqrt{\left(v_x^f \right)^2 + \left(v_y^f \right)^2}$	$\left[m \cdot s^{-1} \right]$
$\tau_{xx}, \tau_{yy}, \tau_{xy}$	Deviatoric stresses	$[Pa]$
τ_{II}	$= \sqrt{\tau_{xx}^2 + \tau_{xy}^2}$	$[Pa]$
k	Permeability	$\left[m^2 \right]$
η_f	Fluid viscosity	$[Pa \cdot s]$
η_s	Shear viscosity solid	$[Pa \cdot s]$
λ	Bulk viscosity solid	$[Pa \cdot s]$
K_s	Bulk modulus solid	$[Pa]$
K_d	Bulk modulus drained	$[Pa]$
p_{ini}	Initial ambient pressure	$[Pa]$
$\bar{D}_{xx}$	Far-field deformation rate	$\left[s^{-1} \right]$
r	Bandwidth of Gaussian	$[m]$
w	Model width	$[m]$

1029